**Ana Luís Cerqueira
Brinca Moreira**

Desenvolvimento de biossensores impedimétricos de grafeno induzido por laser para a deteção de *Escherichia coli*

Development of laser-induced graphene impedimetric biosensors for *Escherichia coli* detection

Ana Luís Cerqueira Brinca Moreira

Desenvolvimento de biossensores impedimétricos de grafeno induzido por laser para a deteção de *Escherichia coli*

Development of laser-induced graphene impedimetric biosensors for *Escherichia coli* detection

Dissertação apresentada à Universidade de Aveiro para cumprimento dos requisitos necessários à obtenção do grau de Mestre em Engenharia Física, realizada sob a orientação científica da Professora Doutora Florinda Mendes da Costa, Professora Associada do Departamento de Física da Universidade de Aveiro, Professora Doutora Isabel da Silva Henriques, Professora Auxiliar do Departamento de Ciências da Vida da Faculdade de Ciências e Tecnologia da Universidade de Coimbra, e da Doutora Sónia Oliveira Pereira, estagiária de pós-doutoramento do Departamento de Física da Universidade de Aveiro. Este trabalho foi realizado em parceira com a empresa Bosch Termotecnologia S.A. Aveiro, sob a supervisão da Doutora Alexandra Gonçalves.

"[...] invejo aqueles que venham a saber mais, mas sei que, tal como eu, terão que medir, pesar, deduzir e desconfiar das deduções alcançadas, distinguir o que há de falso no verdadeiro e levar em conta a eterna mistura da verdade e da falsidade."

In, Marguerite Yourcenar, *A Obra ao Negro*

o júri

presidente   Prof. Doutor Vítor José Babau Torres
                                        Professor Catedrático do Departamento de Física da Universidade de Aveiro

orientadora   Prof.ª Doutora Florinda Mendes da Costa
                                        Professora Associada do Departamento de Física da Universidade de Aveiro

arguente   Doutora Rosa Sofia Rodrigues Teixeira
                                        Investigadora Auxiliar do Instituto Nacional Tyndall da Universidade de Cork

agradecimentos

Em primeiro lugar, gostaria de agradecer à Professora Doutora Florinda da Costa, à Professora Doutora Isabel da Silva Henriques e à Doutora Sónia Oliveira Pereira pela orientação e apoio que incansavelmente proporcionaram ao longo deste percurso, contribuindo não só para o crescimento e desenvolvimento deste trabalho, mas também para o meu, tanto em termos pessoais como profissionais.

Da mesma forma, quero agradecer ao Doutor Nuno Santos por toda a partilha de conhecimento e experiência sem a qual este trabalho não teria chegado tão longe.

Ao Dr. António José Fernandes e ao Alexandre quero agradecer pela disponibilidade e paciência para as minhas dúvidas e inabilidades científicas. Também gostaria de agradecer à Célia por toda a ajuda no manuseamento do laser.

A todo o grupo de trabalho um enorme obrigada pelo tempo, paciência e espírito crítico constantes, que marcaram a minha força motriz no desenvolvimento desta tese e no meu percurso.

Agradeço também à Doutora Alexandra Gonçalves e à Bosch Termotecnologia, S.A. Aveiro pelo apoio dado durante o desenvolvimento deste trabalho.

Quero agradecer a todos os meus amigos engenheiros pelo companheirismo e convívio que me ajudaram a levantar, tantas vezes, durante estes seis anos.

Quero igualmente agradecer ao pessoal do RiaCafé por me ter acompanhado ao longo deste percurso, proporcionando o melhor ambiente para a produção deste documento.

Por fim, um enorme obrigada à minha família, particularmente, aos meus pais e avós pela sabedoria e pelo apoio incondicional que me guiaram até aqui.

palavras-chave

Grafeno induzido por laser (LIG); biossensor eletroquímico; *Escherichia coli* (*E. coli*); imunossensores impedimétricos

resumo

No presente trabalho, pretende-se desenvolver imunossensores impedimétricos à base de grafeno induzido por laser (LIG) para deteção de *E. coli*. Este estudo foi desenvolvido em colaboração com a Bosch Termotecnologia, S.A. Aveiro, no âmbito do projecto *Smart Green Homes* em co-promoção.

Primeiramente, procedeu-se à produção de elétrodos de LIG, explorando o efeito da velocidade de varrimento do feixe laser, v_{laser}, sobre a folha de poliimida (Kapton®). Para tal, foram estudados 5 valores: 150, 200, 250, 300 e 350 mm/s. De forma a comparar o efeito das diferentes velocidades de varrimento, foi realizada uma caracterização abrangente através das técnicas de espetroscopia de Raman, microscopia eletrónica de varrimento (SEM) e caracterização eletroquímica, definindo as respetivas constante de transferência de carga heterogénea, k^0, área eletroquímica efetiva, A_{eff}, e capacitância por unidade de área, γ_{dl}. De acordo com os resultados obtidos, a amostra de LIG produzida com 250 mm/s foi selecionada para continuar o trabalho, nomeadamente, a funcionalização. Para tal, a amostra foi analisada por espetroscopia de fotoeletrões excitados por raios-X (XPS).

O protocolo de funcionalização foi estudado por espetroscopia de impedância eletroquímica (EIS) e voltametria cíclica (CV). O processo de funcionalização foi dividido em quatro passos: hidroxilação, silanização de APTES, funcionalização covalente do anti-*E. coli* e passivação com BSA. Em particular, foi estudada a necessidade de hidroxilar os elétrodos de LIG recorrendo à espetroscopia de Raman, XPS e à respetiva caracterização eletroquímica (k^0, A_{eff} and γ_{dl}). Além disso, também foi considerado relevante, para compreender os resultados obtidos através de EIS e CV, realizar a caracterização eletroquímica das amostras silanizadas com APTES. Deste modo, foi possível estabelecer um protocolo de funcionalização apropriado à aplicação em vista.

A resposta dos biossensores desenvolvidos foi testada através de medidas de EIS, utilizando 7 concentrações de *E. coli* (5, 10, 10^2, 10^3, 10^4, 10^5, 10^6 CFU/mL). Nestes testes também foram contemplados controlos para determinação de falsos-positivos e seletividade. Contudo, os resultados obtidos foram inconclusivos relativamente à deteção de *E. coli*, levando ao planeamento de novos testes. Desta forma, recorreu-se a duas estirpes de *E. coli* e a testes de EIS, de DNA bacteriano e análise de SEM, com os quais se provou que os sensores produzidos são capazes de detetar *E. coli*.

keywords

Laser-induced graphene (LIG); electrochemical biosensor; impedimetric immunosensor; *Escherichia coli* (*E. coli*)

abstract

In this work, it was intended the development of a laser induced graphene (LIG) impedimetric immunosensor for *Escherichia coli* detection. This investigation was explored in cooperation with Bosch Thermotechnology S.A. Aveiro within the co-promoted *Smart Green Home* project.

To start, LIG electrodes were produced, fixating all the laser parameters with exception of the laser scan speed, v_{laser}, for which five values (150, 200, 250, 300 and 350 mm/s) were explored. A comprehensive study to compare the five v_{laser} was done through Raman spectroscopy, scanning electron microscopy (SEM) and determination of the respective electrochemical parameters: heterogeneous charge transfer rate constant, k^0, effective electroactive area, A_{eff}, and capacitance per unit area, γ_{dl}. As a result, the sample produced with 250 mm/s was chosen to proceed with functionalisation, being subjected to X-ray photoelectron spectroscopy (XPS).

Afterwards, a four steps functionalisation, comprehending hydroxylation, APTES silanization, anti-*E.coli* covalent immobilisation and BSA passivation, was studied through electrochemical impedance spectroscopy (EIS) and cyclic voltammetry (CV). Particularly, it was explored the need to perform hydroxylation using Raman spectroscopy, XPS and determination of the corresponding k^0, A_{eff} and γ_{dl}. Also, in the case of APTES silanization, it was relevant to establish the respective k^0, A_{eff} and γ_{dl} to better understand the EIS and CV measurements. Consequently, a suitable functionalisation protocol was achieved.

Lastly, the biosensing response of the produced biosensors was investigated by EIS towards 7 *E. coli* concentrations (5, 10, 10^2, 10^3, 10^4, 10^5, 10^6 CFU/mL). These tests also comprised false-positive and selectivity controls.

However, the obtained results were inconclusive regarding *E. coli* detection, so a set of confirmatory tests was established using two strains of *E. coli* to verify the efficiency of antibody-antigen interaction. To prove *E. coli* detection, the biosensors, upon bacteria immobilisation, were submitted to EIS measurements, bacterial DNA tests and SEM analysis. In fact, *E. coli* detection was confirmed.

Table of Contents

List of Figures

List of Tables

List of Acronyms and symbols

AC – Alternate current
APTES – (3-aminopropyl)triethoxysilane
BDD – Boron-doped diamond
BSA – Bovine serum albumin
CC – Chronocoulometry
CCD – Charge coupled device
CE – Counter electrode
CNT – Carbon nanotube
CFU – Colony forming unit
CPE – Constant phase element
CV – Cyclic voltammetry
CVD – Chemical vapor deposition
DC – Direct current
DI – Deionised
EDC – N-(3-dimethylaminopropyl)-N'-ethylcarbodiimide hydrochlorine
EIS – Electrochemical impedance spectroscopy
ELISA – Enzyme-linked immunosorbent assay
FET – Field effect transistor
FGS-ML – Functionalised graphene sheets monolayer
GC – Glassy carbon
GF – graphene foam
GO – Graphene oxide
HOPG – Highly-oriented pyrolytic graphite
LA – Luria Bertani medium supplemented with agar at 1.5%
LB – Luria Bertani medium
LIG – Laser induced graphene
LOD – Limit of detection
LOQ – Limit of quantitation
MG – monolayer graphene
MF – Membrane Filtration
MTF – Multiple Tube Fermentation
MNP – Magnetic nanoparticle
MPN – Most Probable Number
MWCNT – multi-walled carbon nanotubes
NHS – N-hydroxysuccinimide
NP – Nanoparticle
OCP – Open circuit potential
OD – Optical density
PBS - Phosphate Buffer Saline
PC – Plate Count
PCR – Polymerase chain reaction
PI – Polyimide

RE - Reference electrode
rGO - Reduced graphene oxide
rGS – reduced graphene sheets
SEM – Scanning electron microscopy
SWCNT – Single wall carbon nanotube
WE - Working electrode
XPS – X-ray photoelectron spectroscopy

A_{eff} – Electrochemical effective area
C – Concentration
C_{dl} – Double-layer capacitance
D – Diffusion coefficient
d – distance between lines of laser scanning
E – Potential
F – Faraday's constant
f – Frequency in Hz
h – distance between the laser head and the PI sheet
I or i – Electric current
I_D – Raman D band intensity
I_{2D} – Raman 2D band intensity
I_G – Raman G band intensity
J – Current density
j – Imaginary unit
k^0 – Heterogeneous charge transfer rate constant
P_{laser} – Laser power output
R – Universal gas constant
R_{CT} – Faradaic charge transfer resistance
R_S – Series ohmic resistance
S – Sensitivity
T – Temperature
t – Temporal coordinate
v_{laser} – Laser scan speed
Z – Impedance
Z_{Im} – Imaginary component of the impedance vector
Z_{Re} – Real component of the impedance vector
Z_W – Warburg impedance
α – charge transfer coefficient
$γ_{dl}$ – Capacitance per unit area
$ν$ or v_{CV} – Voltammetric scan rate
ϕ – Phase angle
Ψ – Nicholson's kinetic function
ω – Angular frequency

1 | Introduction

"Ensure availability and sustainable management of water and sanitation for all" was established as 6th of 17 goals to achieve in *The 2030 Agenda for Sustainable Development*. This goal is directly related to others of the agenda, as eradication of poverty and hunger, since water quality, as well as potable water quantity, is completely indispensable to human health and development [1]. The World Health Organisation (WHO)/United Nations Children's Fund (UNICEF) Joint Monitoring Programme (JMP) for Water Supplies has estimated that, in 2012, at least 1.8 billion people globally used a source of drinking water that is faecally contaminated [2]. Hence, the program assigned as its highest priority, towards water quality, the identification of faecal contamination in drinking water. For that matter, it is standardised the detection of the indicator bacteria *Escherichia coli (E. coli)* [2]–[4].

Despite the fact that legislation globally and WHO's Guidelines for Drinking-Water Quality are very strict on the absence of *E. coli* in 100 mL water sample, the quantification of this organism allows a clearer evaluation of the water treatment being implemented and the health risk amplification. Obviously, if the enumeration method is sensitive to very low concentrations of *E. coli* (e. g. 1-10 CFU/mL) it means that is able to detect very small quantities, which usually is difficult to analyse through the presence/absence detection tests [2].

Nowadays, the detection and quantification of *E. coli* still resorts to traditional culture-based methods that have well-known and reliable protocols, but are very time-consuming (2-3 days) and usually need qualified personnel and prepared installations to perform it [3], [5]. Yet, during the past century, progresses had been made both on detection and quantification methods. In terms of detection, biochemical assays have shown capable protocols for bacteria detection leaning on enzymatic and molecular approaches [6]. Nevertheless, enzymatic techniques are still very time-consuming and dependent on competent workers and convenient laboratories. Although molecular techniques improve significantly the time concern, it demands sample preparation and specific reagents, which clearly depends upon laboratory specificities and workers and higher costs [5]–[8].

Therefore, the new promising trend that targets all the issues mentioned before are the biosensors. Biosensors are defined as devices able to biologically recognise a target molecule by a biochemical element that is linked to the transducer, which is responsible for convert the biological recognition into a detectable and/or measurable signal that adjusts accordingly to the quantity of the target bioanalyte detected [5], [7], [9]–[12]. As a result of its definition, biosensors can be categorised by the biological sensing element (e.g. enzyme, antibody, DNA) and by the type of signal produced by the transducer (e.g. electrochemical, optical, electric, mechanical, etc.) [5], [9]. Consequently, research on biosensors complies the characterisation of the transduction component and its suitability on the proposed application as well as the study of the most convenient functionalisation for the proper biorecognition [13], [14]. Both studies are necessary to obtain biosensors with significant selectivity, sensitivity, reliability, portability, real-time analysis, simplicity of operation and reduced costs [15].

Electrochemical biosensors are currently one of the main attractions on the biosensors universe due to the ease for miniaturisation of the whole device, which allows for point-of-care testing, no need sample preparation, fast time response, high sensitivity and low costs of production. More specifically, impedance-based electrochemical biosensors highlight the aspects mentioned above,

especially in the case of bacteria detection [5], [10], [13], [14], [16]–[18]. High specificity can be attained with a convenient biorecognition element, that in cases of bacteria depends upon the target analyte. In other words, if it is intended to detect the bacteria itself, an antibody or aptamer can be used. In the case of a metabolic product detection, which indirectly represents its presence, enzymes or other specific proteins are frequently used. As far as sensitivity is concerned, it is important to use materials that have electrochemical stability, high electron transfer rate, large surface area and also manifest low currents in an electroactive species-free electrolyte solution over a wide potential window [13], [19]. Therefore, it is common to use metals, metal-oxides, organic conductive polymers and carbon-based materials as transducer for electrochemical biosensors. More recently, nanomaterials such as graphene, carbon nanotubes and nanoparticles have been studied to improve the sensitivity, selectivity and reliability of biosensors [13], [19]–[22].

Regarding carbon-based materials, the popularity ascribed to graphene due to its unique properties has opened horizons to improve technological applications. However, large-scale production of such nanostructure remains very expensive and time consuming. To overcome these drawbacks, new techniques have been studied and developed to produce graphene in order to preserve high quality aspects, such as the absence of defects and being single-layer. Consequently, the resultant structures are inserted in the category of graphene-based materials [20]–[22].

In electrochemical applications, the advantages and disadvantages that some of these graphene-based materials present relative to pristine graphene have been studied. Interestingly, regarding electron transfer rate, graphene-based electrodes have been shown to provide higher values and, consequently, are more suitable for impedance-based biosensing [23]–[25].

Nonetheless, the synthesis of graphene-based structures involves multiple steps protocols and/or exhaustive thermal conditions, what recedes the commercial impact of graphene-based materials.

In 2014, Tour's group presented a one-step process to obtain porous graphene-based structures from a polymer sheet [26]. This process consisted on the incidence of a CO_2 laser beam on a polyimide sheet at atmospheric conditions, which generated a photothermal reaction on its structure and resulted in a 3D graphene-based material designated by laser-induced graphene (LIG) [26]. Additionally, this process enabled the synthesis of flexible, patternable and scalable graphene-based structures, amplifying its applications in supercapacitors, flexible electronics and biosensors.

In this thesis, it is explored the development of a LIG electrode to detect *E. coli* for a label-free immunological impedimetric biosensing system. The purpose of the system is to analyse faecal-contamination in water samples.

Therefore, in Chapter **II**, some concepts, principles and methodologies relative to *E. coli* detection and biosensors are explored. Also, a brief state of the art is reviewed regarding graphene-based materials in electrochemical applications and LIG development. In **Chapter III**, the whole experimental procedure is displayed, beginning with LIG production and ending with tests for *E. coli* detection. In **Chapter IV**, it is introduced a comprehensive characterisation of the LIG electrodes through its morphology, composition and electrochemical properties. Consequently, the steps for complete functionalisation of the electrode are covered, from hydroxylation to passivation steps. Finally, tests for *E. coli* detection are analysed and discussed. The conclusion remarks and suggestions as future work are undertaken on the final **Chapter V**.

2

II | Fundamentals and Technological Background

2.1 *Escherichia coli* detection

E. coli and faecal-contaminated water

Usually, to assess drinking-water quality and effectiveness of the cleaning treatments, the total coliforms are among the most used indicators [3]. This group comprises bacteria belonging to the genera *Escherichia, Enterobacter, Klebsiella* and *Citrobacter* and some species that belong to genera such as *Serratia, Hafnia, Leclercia*, among others [6], [27]–[29]. These are, indeed, included in the *Enterobacteriacea* family. Consequently, total coliforms behold facultative aerobic, non-spore forming, rod-shaped, gram-negative bacteria able to ferment glucose [27], [28]. Among other morphological and metabolic characteristics, this family is also well-defined by the presence of enterobacterial common antigen (ECA) and, most importantly, by some gene sequences common within the *Enterobacteriacea* family [27].

The total coliforms distinguish from the rest of the *Enterobacteriacea* family by the abilities of producing the enzyme beta-galactosidase and fermenting to acid and gas, along its growth at 35-37 °C. However, the total coliforms group is heterogeneous and presents bacteria that grow in animal and human colon (feacal source) and some can also survive and grow in other nutrient-rich environments (soil and water). Some of these non-faecal bacteria are tolerated in some types of water and their detection is not conclusive of faecal contamination. Therefore, the detection of faecal contamination cannot rely on the detection of total coliforms [3], [29]–[31].

Among total coliforms, it is appropriate to distinguish the thermotolerant bacteria that are known for fermenting lactose at 44-45 °C. Although *Escherichia coli* makes part of this subgroup, outstands by the capability of producing indole from tryptophan and the enzyme beta-glucuronidase [6], [29]. Also, *E. coli* remains the only bacteria within the group that is originated only from faeces. Hence, it is extremely relevant to identify *E. coli* species as a reliable faecal indicator since is very abundant in intestines of human and other warm-blooded animals and is very rarely found in non-faecal polluted environments [3], [32], [33]. Therefore, *E. coli* can be characterised separately from the other coliform bacteria and so, it can and should be distinguishably detected, too.

E. coli current detection methods

Culture-based methods are still the most used regarding bacteria detection in water [34]. These include techniques such as Multiple Tube Fermentation (MTF), Most Probable Number (MPN), membrane filtration (MF) and plate count (PC) methods. Essentially, these methods demand inoculation and incubation of the harvested sample on selective differential and/or broth media, for a convenient growing time interval, at a suitable temperature, stimulating growth of the bacterial colonies. Consequently, in the case of coliform bacteria, for each of these methods the evaluation is determined by the products regarding lactose fermentation. In the case of *E. coli,* the detection usually relies on the expression of the *beta*-glucuronidase [35].

For instance, in the MTF technique, the water sample is diluted in a series of tubes with culture medium broth supplemented with lactose. After growth, e. g. at 45 °C for 24 hours regarding

thermotolerant coliforms, it is aimed to evaluate a change in colour, indicating the production of acids resultant from lactose fermentation, as well as the presence of gas bubbles, expressing gas production. This method involves three steps, presumptive, confirmatory and completed tests, which will produce a pattern of detection, regarding the dilution and by analysis of statistical tables is possible to determine the most probable number of bacteria in the original sample [6].

Plate count methods also require several dilutions of the water sample, that are poured into Petri dishes with suitable medium and are incubated at growing constrains. Then, the viable cells multiply arising what is named colony-forming units (CFU) which can be detectable by the naked-eye, enabling its count that is correlated to the number of bacterial cells in the original sample [36]. Similarly, the membrane filtration method only contrast with PC methods on the initial step of the procedure. In fact, the MF requires the water sample to be filtrated through a sterile membrane filter with porous size ranging from 0.2 to 0.45 μm. Then, the filter is inoculated to a culture medium, in a Petri dish, and follows the rest of the steps described for the PC methods [6].

Culture-based methods are reliable for detection and enumeration of bacteria [35], [37], [38]. However, besides being very time-consuming, taking 2 to 3 days, the methods require specialised workers and installations. In order to reduce the test time, molecular methods relying on detection of bacteria characteristics, instead of its metabolic products, had been developed. These methods should focus on bacteria features that specifies well the strain under evaluation without the demand of confirmation tests. Immunological tests, based on the interaction between antibodies and the specific correspondent antigen, and nucleic acid-based methods, based on the hybridisation of complementary nucleic acids, were developed [6].

Enzyme-linked immunoabsorbent assay (ELISA) leans on the use of antibodies to specifically detect antigens of bacteria. Generally, this method comprises a microtiter plate where antigens are immobilised, which can be executed with a primary antibody, and then are spotted by an antibody that is linked to an enzyme, in which its purpose is to catalyse a substrate reaction producing a luminescent or colorimetric signal, that constitute the signal of detection. The most common way to perform this technique in a "sandwich"-like method. Also, instead of an enzyme linked to the secondary antibody, it is typical to use a fluorochrome [6], [39].

Polymerase chain reaction (PCR) takes advantage of DNA-DNA and DNA-RNA hybridisations to perform identification and detection of bacteria. Firstly, the technique requires an extraction of the DNA or RNA content of the bacteria (normally, by bacterial lysis) followed by its denaturation (from double- to single-stranded). Secondly, it compels the use of primers which are single-stranded oligonucleotides that will link to the denaturated DNA. At specific temperature conditions, the hybridisation reaction occurs between complementary strands. Thirdly, PCR includes an amplification step, in which replication of the target DNA sequence is performed. Amplification relies on an enzyme, DNA polymerase, that catalyses the replication. Lastly, the detection process can be achieved by electrophoresis of the amplicons, visualised by labelling the primer with a fluorochrome or staining the amplification products [6], [40].

Both techniques do not require pre-enrichment of the sample (inoculation and incubation), decreasing the time requested for detection from days to hours, but still require qualified workers and specific laboratory materials and conditions, what, besides summing costs to the process, are not user-friendly.

In fact, the principles of ELISA and PCR methods can be recovered for biorecognition events that combined with a structure ready to translate the produced phenomenon to a measurable signal (transducer), in a wise time set, gives rise to the biosensor device.

2.2 Biosensors: principles and methodologies

A biosensor is a device that allows detecting and/or quantifying the presence of a certain analyte (protein, bacteria, virus, etc.) in a given matrix (blood, water, food, etc.). For that matter, these devices are composed of two very important components. The first, the bioreceptor that is responsible to link or react with the analyte to be detected or an analyte component. The second, the transduction electrode that can produce a signal as a consequence of the stimulus generated by the biorecognition event, whether if it is a reaction or a bound (**Figure 2.1**).
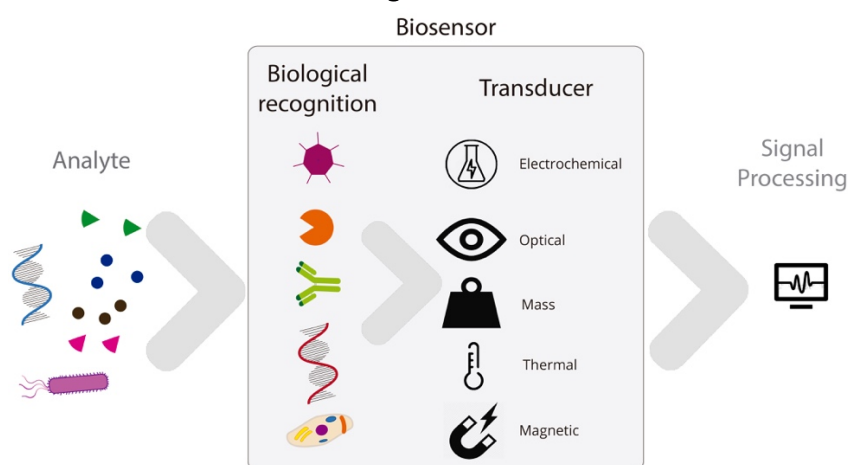
Figure 2.1: Representative scheme of biosensor, including the stimulus flow from the analyte to the signal processing stage.

Bioreceptors

The biochemical recognition element can characterise the type of detection addressed to the device, and for the choice of the bioreceptor, it is critical to have in mind the analyte to be detected, specially, since this element is responsible for the selectivity of the biosensor [10]. Bioreceptors can be displayed by antibodies, enzymes, nucleic acids, proteins, viruses or cells [41]. Fundamentally, the recognition can be induced by biocatalytic events or by an affinity mechanism, both between the receptor and the analyte.

In the case of **biocatalytic events**, the biorecognition element assumes a catalyst role on the analyte, stimulating the rate of a characteristic chemical reaction (that can be metabolic) and consequently, enabling a fast production of specific molecules that are detectable by the transducer, e. g. electroactive species, gas [10], [41]–[43]. Usually, this biocatalytic recognition is performed by enzymes, but it can also be executed by cells or tissues. Indeed, the enzymatic approach is the oldest and most studied one, it is a simple, inexpensive with high specificity biorecognition method [10], [43]. The application of this method recalls the birth of biosensors, which is associated with the presentation of a system based on electrochemical sensors for monitoring blood constituents by Clark and Lyons [44]. In this work, an oxygen sensor was combined with an enzymatic membrane that catalysed the oxidation of glucose, which generates oxygen, allowing a reading of glucose concentration [44].

In the case of **bioaffinity mechanism**, the recognition settles on binding interaction between the biorecognition element and the analyte or analyte component. Generally, affinity-based recognition embraces antibody-antigen interaction, DNA hybridisation and receptor-protein (non-catalytic and non-immuno enzymes) affinity [42], [45]. However, the latter implicates more complexity, specifically in isolation of such receptor-proteins [45], [46]. As a matter of fact, affinity-based biorecognition presents simple, selective and sensitive detection methods, since, in the case of antibodies, these bioreceptors are chosen to recognise an antigen which are usually proteins [42], [45]. In the case of DNA sequences, it is intended that the binding will only occur if the target analyte has the complementary sequence [42], [45]. So, indeed, affinity-based techniques are very specific. The most common and reliable bioaffinity technique is antibody-antigen interaction. Even though this binding is non-covalent, it is very strong and is extremely selective [42], [45].

In addition, another classification arises from the biorecognition event based on the necessity of a label element essential to the detection. In other words, the biorecognition event might not depend only on one bioreceptor, but also on a second that has an integrated tag, like a luminescent or magnetic particle, that will label the analyte for detection, in a "sandwich"-like method. Accordingly, biosensors can be label-free or label-based, establishing whether the detection is direct or indirect.

Transducers

The transducer defines the type of signal analysis inherent to the device. For this matter, it is relevant to keep in mind the type of biosensing approach, meaning if it is a direct or indirect detection, the biorecognition technique and, specially, what type of material used in the transduction component. Transducers are classified based on the type of measurable signal produced under the biorecognition event. This signal can manifest in terms of luminescence, reflectance, mass, temperature, potential, current and impedance, among others. Hence, the classification of the biosensors, accordingly to the transduction mechanism, can be generally divided into optical, mechanical, thermal, magnetic and electrochemical transducers.

Optical Biosensors | The optical signal, consequent from the interaction between the bioreceptor and the analyte, can be displayed by direct interaction of the analysed analyte with the transducer's surface or by the use of a colorimetric or luminescent element that labels the recognition [5], [47]. The direct detection is label-free and benefits from several optical phenomena, such as surface plasmon resonance, evanescent wave, Raman-scattering interferometric and ellipsometric spectroscopy, among others [47], [48]. In the label-based case, the colorimetric or luminescent tag can be integrated on the bioreceptor itself or on a second bioreceptor that will interact only with the analyte molecules that were recognised and induces a colorimetric or luminescent signal, respectively.

Mechanical Biosensors | Generally, these biosensors depend on a (micro)cantilever element that, upon recognition of target analyte on its surface, can have two different behaviours. In the case of a quasistatic cantilever, biorecognition triggers surface stress inducing the cantilever to deflect. In the case of a dynamic device, the cantilever oscillates at a resonance frequency that modulates when biochemical binding events take place [49]. There is also the Piezoelectric Quartz Microbalance which operation is equivalent to the dynamic microcantilever, but with quartz crystal as the sensing probe [49].

Thermal Biosensors | The transducers of such biosensors are consistently thermistors, which fundamentally are resistances whose value is dependent on temperature. Therefore, along with a

catalytic event of biorecognition, absorption or release of heat occurs, changing the temperature of the sample. The latter provokes a change in the resistance [50], [51].

Magnetic Biosensors | Since most biological samples do not present significant magnetic susceptibility, integration of magnetic nanoparticles into biorecognition elements enables the detection of biological analytes through magnetic transducers. Indeed, the magnetic particles work as labels that will be detected by magnetometers, such as superconducting quantum interference device (SQUID), magnetoresistive sensors and hall-effect sensors [52].

Electrochemical Biosensors | The transducers are electrodes that generate an electric response as a consequence of a biochemical reaction or affinity linkage between the analyte and the biorecognition element on the surface of the electrode [53], [54].

The general principle of biosensors allows one to establish a relation between the concentration of the target analyte (input) and the signal generated by its recognition (output), under certain conditions. This relation can be settle by means of a calibration curve, including the correspondent measurement uncertainty [55]. As demonstrated above, the biosensing universe embodies a very large scope of operation systems, constraining direct comparison between them. So, regarding the output signal and respective calibration curves, some figures of merit were established by the International Union Of Pure And Applied Chemistry (IUPAC) to validate and provide a general consensual basis to confront devices and systems [55], [56]. Some of the most convenient are shown in **Table 2.1**.

Table 2.1: Some of the most convenient figures of merit for biosensors performance analysis defined by IUPAC [55], [56].

Linear range	It confines the concentration values for which the calibration function is linear.	-
Dynamic range	It defines the absolute limits of concentration that can be detected.	-
The limit of detection (LOD)	It states the minimum concentration value that the device can measure. Meaning, the lowest concentration value for which the output signal is distinguishable from the signal generated in absence of analyte (s_B), with a reasonable certainty (k=3).	$LOD = s_B + k\sigma$ $k = 3$
The limit of quantitation (LOQ)	Similarly to LOD, it designates the minimal analyte concentration for which the originated response can be reliably determined, with great certainty (k=10).	$LOQ = s_B + k\sigma$ $k = 10$
Sensitivity	It is the slope of the calibration curve, indicating that as greater the ratio between the output signal (Δs) and the correspondent concentration (ΔC) of the analyte can be, the easier it is to distinct the response from two very close concentrations.	$S = \dfrac{\Delta s}{\Delta C}$
Analytical sensitivity	It is represented by the ratio between the sensitivity (S) and instrumental noise (n). Along with this parameter, its reciprocal value defines the minimum concentration variation, within the linear range.	$S_a = \dfrac{S}{n}$
Selectivity	It is determined by the ratio between the signal produced by the target analyte and the signal generated by interference elements, which can be crucial to validate the device ability to detect the analyte on a complex matrix.	-

σ – standard deviation of the signal.

To accomplish their function, a strategy of the whole biosensor development should be traced, knowing which analyte to detect and which material to use for transducer fabrication, choosing the biorecognition element and what type of detection signal generated for detection. With respect to the goal proposed in this thesis, it is clear the intention to detect the bacteria *E. coli*. Consequently, it was selected the antibody-antigen affinity approach for recognition of the bacteria, since it presents ease in immobilisation, high levels of selectivity and stability [57] and, particularly, it allows a detection approach that recognizes the whole cell without the need for lysis or extraction of inner-cell components [5]. Regarding the transducer element, the goal was to implement a graphene-based material with a fast and cost-effective synthesis. Therefore, the more suitable response system seemed the electrochemical branch of transducers.

Electrochemical Biosensors

Electrochemical biosensors became the most commercially developed category of biosensors largely due to the fame and success ascribed to glucose detection, for diabetes monitoring.

The general working principle of electrochemical biosensors depends on the generation or consume of electrochemical species (ions or electrons), as consequence of the biorecognition event, that originate a signal that can be translated by potentiometric, amperometric, conductometric, field-effect transistors and impedimetric transducers [53]. Frequently, these systems use an electrolyte, as the mean for the measurement, and a three electrodes setup, settling the electrochemical cell. The latter is composed by a working electrode (WE), where the sensing event occurs, a reference electrode (RE), whose function is to bear a known and stable potential, and a counter electrode (CE), responsible to establish the connection with the electrolyte [58].

Potentiometric biosensors frequently use ion-selective, pH or gas electrodes for transducing the biochemical event of recognition [59]. The measurements are taken under equilibrium conditions at open-circuit. The signal is the potential (also named electromotive force, EMF), between the WE and RE, created by the accumulation of charges (ionic species) on the WE interface. Hence, the potential generated (E) has a logarithmic relation to the analyte concentration that is described by the Nernst equation,

$$E = E^0 - \frac{RT}{z_i F}\ln(a_i),$$

(eq. 2.1)

in which E^0 is a constant potential contribution, R the universal gas constant, T the absolute temperature, F the Faraday's constant, z_i the charge of the detected ion and, finally, a_i the ion activity [58]. The a_i parameter is the product of ion concentration and the ion mean activity coefficient, which for very diluted solutions is equal to one [60].

In contrast, **amperometric devices** measure the current generated by oxidation or reduction of an electroactive species, resulted from biochemical recognition of the analyte. These devices perform on a fixed potential, or by scanning a range of potentials set between the WE and RE, corresponding to amperometry or voltammetry techniques, respectively. Regarding amperometry, the current peaks, generated by the redox reaction, have a linear proportionality with the analyte concentration, described by

$$i = nFk^0C$$

(eq. 2.2)

where n is the number of electrons implicated in the reaction, F the Faraday's constant, k^0 the heterogeneous electron transfer rate constant and C the analyte concentration [58], [61].

Field-effect transistor (FET) biosensors resemble in components and performance to regular FET device. Likewise, it is a transistor, with two metallic electrodes, the source and drain, and a semiconducting channel, linking both electrodes, through which charge carriers flow. The current flowing from the source to the drain depends on the potential applied at the gate electrode, on top of the channel. The potential creates an electric field across the channel, controlling the current. In biosensing technology, the gate potential is designated by the reference electrode, which is located above the sensing electrode, carried out by the channel. Upon biochemical interaction with the analyte, the charge distribution changes the charge carrier density on the channel and, consequently, the current flowing on it. Thus, it enables the detection through a linear relation between analyte concentration and source-drain conductivity [23].

In the case of **conductometric biosensors**, the reference electrode is dispensed. As a matter of fact, the principle of performance of these devices leans on changes of conductivity between two electrodes. The measurements take place in a solution where, usually, the biorecognition is performed by an enzyme. The latter reacts with the analyte and, consequently, alters the concentration of charged species in the solution between the electrodes [42], [58], [62]. This approach is not suitable for matrixes with high ionic-background, such as in clinical assays. In alternative, conductometric measurements can be applied to monitor changes in the surface of an electrode by means of biorecognition [58].

Lastly, **impedimetric biosensors** recall impedance-based measurements, which permit the characterisation of electrochemical systems, analysing both interface and bulk electric properties of an electrochemical cell. For that matter, it benefits from techniques such as electrochemical impedance spectroscopy (EIS) that uses the three electrodes configuration immersed in an electrolyte, which is pictured in a scheme presented in section 4.1 (**Figure 3.3**).

The working principle settles on applying a low-amplitude (2-10 mV) sine-wave signal, e, sweeping a range of frequencies, f, to the electrochemical cell, at its open-circuit potential (OCP) or at a pre-defined DC bias.

$$e = E \sin(\omega t), \quad \omega = 2\pi f \qquad \text{(eq. 2.3)}$$

Consequently, this AC perturbation will generate a current response, i, dependent on the frequency of the applied signal with an additional phase shift, ϕ, relative to the imposed signal.

$$i = I \sin(\omega t + \phi) \qquad \text{(eq. 2.4)}$$

The response is read in terms of impedance, Z, which is established by Ohm's law

$$Z(\omega) = \frac{e}{i} \qquad \text{(eq. 2.5)}$$

$$Z(\omega) = \frac{E \sin(\omega t)}{I \sin(\omega t + \phi)} \qquad \text{(eq. 2.6)}$$

The dependence of the current's phase relative to the frequency of the imposed signal concedes a Z phasor behaviour, which can be graphically represented by a Nyquist plot, in which the reactance (imaginary impedance), Z_{Im}, is plotted against the resistance (real impedance), Z_{Re} (**Figure 2.2**-a).

$$Z = |Z|e^{j\phi} \qquad \text{(eq. 2.7)}$$

$$Z = |Z| \cos \phi - j|Z| \sin \phi \qquad \text{(eq. 2.8)}$$

$$Z(\omega) = Z_{Re} - jZ_{Im} \qquad \text{(eq. 2.9)}$$

Generally, these plots enable one to distinguish events occurring in the interface of the WE, for high frequencies, and in the bulk electrolyte, for low frequencies. For a suitable analysis of the system, it is consistently required the appliance of a theoretical model regarding electric circuits. Consequently, one needs to identify the phenomena conceding certain behaviours to the system, define each one of them in terms of electric components, such as resistances and capacitors, and layout the equivalent circuit. Frequently, for impedimetric biosensors, the most commonly fitted is the modified-Randles circuit [63] (**Figure 2.2**-c). Here, the resistance R_S provides the resistivity of the bulk electrolyte, the capacitor C_{dl} models the double-layer capacitance, and R_{ct} reads the resistance of charge transfer on the interface of WE, and finally the Warburg element Z_W describes the diffusion of electroactive species towards the interface of the WE. Experimentally, the electrolyte-electrode interface has a non-ideal capacitor behaviour so, usually, the C_{dl} element is replaced by a constant phase element (CPE) that adjusts its value, accordingly to

$$Z_{CPE} = \frac{1}{P(j\omega)^n}$$

(eq. 2.10)

for which P is analogous to a capacitance and n is a constant modulating the phase of the element, assuming values within 0.5 and 1. For n=1, the constant phase element turns into a true capacitor. Similarly, the Warburg impedance, Z_W, is also a special case of a constant phase element for which the n=0.5, meaning the phase is $\frac{\pi}{4}$ independently of the frequency. Accordingly,

$$Z_W = \left(\frac{2}{\omega}\right)^{\frac{1}{2}} \sigma$$

(eq. 2.11)

where σ is the Warburg coefficient, whose value depends only on the electrolyte.
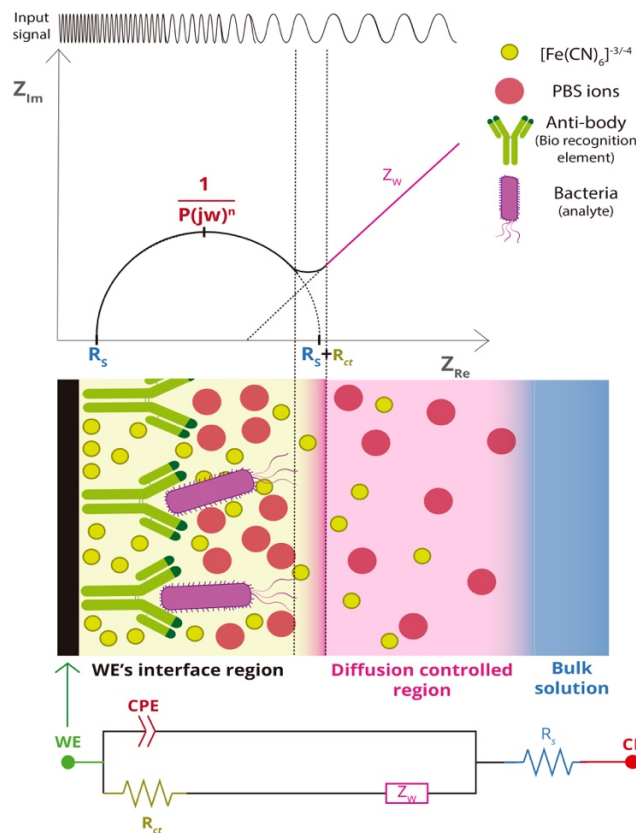
Figure 2.2: (a) Typical Nyquist plot attained with impedimetric faradaic biosensors, for which in (b) there are sketched the corresponding regions on the electrochemical cell and in (c) it is presented the equivalent circuit.

In biosensing, one can distinguish non-faradaic and faradaic biosensors. For the first case, it is common the absence of redox species in the electrolyte, implying that the capacitive behaviour will prevail over the charge transfer on the WE. In this case, the biorecognition event, taking place on the WE, originates a change on the charging of the double-layer capacitor, which permit to obtain a calibration curve of the capacitance relative to analyte concentration. In this case, the equivalent circuit does not integrate a Warburg element and the R_{ct} assumes a value of leak resistance, R_{leak}. In faradaic biosensors, it is mandatory the use of redox species on the electrolyte, since these act as probes for the WE interface. The biorecognition happens exactly as described previously, but its influence is modelled by the charge transfer resistance and the Warburg impedance. For this case, the modified-Randles equivalent circuit fits the best (**Figure 2.2**). Consequently, R$_{ct}$ evolution is linearly proportional to the analyte concentration. Further, this analysis is also very useful to characterise electrodes surface chemical modification.

2.3   Nanomaterials in biosensing

The development of electrochemical biosensors has set on improving its electroanalytical performance, namely sensitivity and selectivity [13]. For that matter, researchers have been intensively working on new strategies for electrodes fabrication. Hence, the introduction of nanomaterials and nanostructures on electrodes development enabled to overcome those challenges [13], [64].

Nanomaterials such as metallic, magnetic nanoparticles and carbon-based materials, mainly carbon nanotubes (CNTs) and graphene, have been applied to electrochemical biosensors, in general, offering advantageous properties commonly associated with its high surface-to-volume ratio, such as enabling larger number of immobilised bioreceptors for sensing purposes [65], [66].

In the case on nanoparticles (NPs), one can resort to metals, metal-oxides, semiconductors and composites [13], [19], [64]. Its functions, in biosensing, relies mainly on immobilisation of biomolecules for analyte recognition, labelling the biorecognition event, providing high catalytic activity and electron transfer and acting as reactant [67]. These result from the unique physical, chemical and electronic properties of such nanomaterials that generally include low dimensions, ranging 1-100 nm, low-background current, high signal-to-noise ratio, fast electron transfer as well as large surface area [19], [67]. Among NPs in electrochemical biosensors, one of the most commonly reported is gold nanoparticles (AuNPs), specially due to its ability, upon biomolecules immobilisation, to retain their bioactivity that improves significantly the sensitivity [64]. Also, in this biosensing category, one can combine magnetic nanoparticles (MNPs) for bioreceptors immobilisation, whether MNPs are integrated into the electrode or dispersed in the sample [13]. The appliance of MNPs allows to take advantage of not only large surface area, but also superparamagnetic property of MNPs which allows selective separation of the target analyte from the sample, enhancing selectivity and detection response speed of the biosensor [13], [19]. For this, it is usual to exploit iron-oxides nanoparticles [52].

Carbon-based materials and electrochemistry

Carbon-based nanomaterials have received special attention regarding electrochemical biosensing, particularly, the nanostructures such as CNTs and graphene. These materials present remarkable high surface-to-volume ratio, high electrical conductivity, chemical stability and

biocompatibility, offering diverse advantages upon integration on electrochemical transducers, as increasing electroactive surface area, enhancing electron transfer and promoting adsorption of molecules [65], [68].

Carbon nanotubes consist on hollow cylinder structures, whose wall can be defined by a single or multi layers of sp^2-hybridised carbon arranged in a honeycomb structure, also known as graphene [68], [69]. Therefore, CNTs can be divided into two categories, single-walled carbon nanotubes (SWCNTs) or multiple-walled carbon nanotubes (MWCNTs), depending if the CNT comprise only one graphene sheet or more than one stacked concentrically [68]–[71]. These present diameters from 0.4 to 2 nm, in the case of SWCNTs, and from 2-100 nm, in the case of MWCNTs, engaging high surface-to-volume ratio [68]. Along with the diameter, SWCNTs' chirality (atomic arrangement) defines the conducting nature of the CNTs, metallic or semiconducting [68], [69], [71]. Accordingly, the electrical properties of SWCNTs vary, in the case of metallic nature it displays conductivities around 1000 times greater than copper, in the case of semiconducting nature, it behaves closely like silicon [69], [72]. Besides, these carbon structures provide high chemical stability, good mechanical strength and, more specifically, CNTs offer fast electron transfer rates, low residual current, wide potential window and high adsorptive ability assuring adequacy for implementation in electrochemical transducers for biosensing applications [13], [68]–[70]. Concerning biosensing, these structures offer both sidewalls and ends to a multitude of options for functionalisation [19], [69]. Additionally, CNTs can be arranged in diverse forms, such as isolated nanotubes, oriented or random planar arrays or even 3D forests, allowing to explore suitability and sensitivity of the desired biosensor [19], [71].

Despite the synthesis of such carbon structures has been well-established by three techniques (arc-discharge, chemical vapour deposition (CVD) and laser ablation [72]), the main issues of implementing CNTs on electrochemical sensing are associated with the following concerns [68], [71]. Firstly, the methods require metallic catalysts, which results in impurities on the CNT structure. Consequently, it becomes necessary to resort to exhaustive cleaning processes to separate the CNTs from the metallic impurities, raising defects on CNTs surface [68], [71]. As a matter of fact, a perfect cleanse is very difficult to achieve, which emerges in the dominant electrochemical activity of these impurities over the CNTs one [68], [71]. Secondly, the synthesis of CNTs always includes both metallic and semiconducting CNTs, demanding once more extra processes for separation (based on selective functionalisation or selective destruction) [68], so that the biosensing surface properties can be properly tailored. Lastly, CNTs have a natural tendency to aggregate through van der Waals interactions, creating bundles [68], which can be beneficial depending on the desired geometrical arrangement and acting function of CNTs [69].

Eventhough there are still some limitations concerning CNTs production, these structures have been extensively studied regarding electrochemical biosensing. The introduction of CNTs in such biosensors is mainly on amperometric and FET-based devices. However, its relevance is not only confined on benefiting sensitivity by its physical properties, but also on providing reliability on biomolecules immobilisation by its outstanding surface chemical properties [13], [19], [68], [71].

Graphene, as already mentioned, is a single layer of sp^2-hybridised carbon atoms arranged in a honeycomb structure. This two-dimensional carbon nanostructure presents high surface area (2630 m^2/g), high carrier mobility at room temperature (~10,000 $cm^2V^{-1}s^{-1}$), good optical transparency (~97.7 %), high Young's modulus (~1 TPa) and excellent thermal conductivity (3000–5000 $Wm^{-1}K^{-1}$) [73]. These unique properties provide its implementation to a wide set of

applications such as electronics, supercapacitors, solar cells, OLED's and biosensing technology [73]–[75].

Graphene was first isolated in 2004 by mechanical exfoliation, meaning repeated peeling, of highly oriented pyrolytic graphite (HOPG) [76]. Indeed, this process enabled the observation and characterisation of graphene sheets for the first time, but in order to obtain pristine graphene this method revealed to be very laborious and not effective for large-scale production. So, since then, the production of large-scale graphene has been on the spotlight of research [74]. Alternatively to mechanical exfoliation, Chemical Vapour Deposition (CVD) [77], epitaxial growth on silicon carbide (SiC) substrates [78], unzipping of CNTs [79] and chemical exfoliation-reduction of graphite oxide [80], [81] are some of the methods that have been explored. Regarding high quality graphene large-scale synthesis, it is considered, nowadays, that CVD is the most promising technique [82]. However, it implies disadvantages as being very expensive and time consuming.

Overcoming these problems, chemical exfoliation-reduction of graphite oxide provides the possibility of producing large-scale graphene-based materials named reduced graphene oxide (rGO) [73]. This method consists of oxidation of graphite, followed by chemical or thermal exfoliation into graphene oxide (GO) sheets that are later submitted to thermal [83], chemical [84], [85] or electrochemical [86]–[88] reduction. The reduction process function as a recover step to eliminate the functional groups originated by the oxidation and, consequently, to regain electric properties more alike to graphene sheets [23], [85]. Consequently, a multi-layer graphene sample is usually obtained presenting not only some functional groups, still from the oxidation, but also a significant amount of defects on the basal plane due to the exfoliation step.

In electrochemistry, it had been studied that, in sp^2 carbon materials, edges have a high rate of electron transfer, while in the basal plane it is incredibly low [24], [25]. So, graphene-based materials, such as rGO, provide enhanced electron transfer, which is a major advantage for electrochemical applications [23]. Besides, the presence of residual functional groups on its structure, such as hydroxyl, contribute for functionalisation and immobilisation of biomolecules on its surface, complying these materials for electrochemical biosensors [89]. Another strategy used to improve immobilisation of biomolecules is to perform this step on GO, since it carries a greater number of functional groups, and then, reduced it electrochemically [90].

For the synthesis of graphene-based materials, novel methods have been emerging in order to reduce the multiple steps (e. g. for rGO) and exhaustive temperatures (e. g. for graphene foams) protocols that recede the commercial impact of these materials. The introduction of one-step cost-effective production of graphene-based materials, resorting to a laser beam and a polymer sheet, raised high expectations on this materials appliance. This technique was based on the photothermal effect produced by the incidence of an infrared (IR) laser beam on the polymer sheet. It was firstly studied for commercial polymer polyimide (PI) [26].

The laser-induced graphene technique was first reported by the Tour group, in 2014 [26]. It consists on induced vibrational perturbations on the lattice of PI through absorption of energy of the radiation, which provokes local increment of temperature. Subsequently, this thermal effect causes rearrangement of the PI structure, breaking and recombining molecular structure. Particularly, this process enables to transform sp^3 carbon on PI into sp^2 carbon [26]. Along with this reaction, gases are liberated, creating a porous structure. This way, a 3D porous graphitic material is grown with PI as substrate and precursor [26]. Further, this technique does not require special atmosphere conditions nor preparation of the PI.

The graphitic material presents graphene-based characteristics and so, it is named laser-induced graphene, LIG. Thus, this process allows to produce a graphene-based material in a fast, simple and cost-effective way, envisioning large-scale production.

LIG has been explored in the past 4 years in terms of promising applications, such as microsupercapacitors [26], [91]–[99], electrochemical [100]–[105] and piezoresistive sensors [106], [107]. In 2016, it was reported the first LIG impedimetric capacitance-based biosensor for detection of bisphenol-A, using aptamer-based biorecognition [101]. Later, in 2017, also using aptamers as bioreceptor, a LIG amperometric biosensor for thrombin detection was developed [108]. In 2018, three more LIG biosensors were documented: two enzyme-based amperometric devices, one detecting biogenic amines in food samples [109] and another glucose [104]; one in which the biorecognition element, Eriochrome black T, was molecularly-imprinted to detect chloramphenicol through Electrochemical Impedance Spectroscopy (EIS) [110].

In this thesis, we present a proof-of-concept of LIG as biosensor for bacteria detection, specifically for *Escherichia coli*, using specific antibodies as biorecognition through EIS technique. In order to present a very brief state of the art of dominantly EIS-based immunosensors for *E. coli* detection, some relevant examples are introduced in **Table 2.2**, endeavouring to acknowledge suitable graphene-based devices.

Table 2.2: Brief list of mainly EIS-based immunosensors for *E. coli* detection, endeavouring to acknowledge suitable graphene-based devices.

Electrode	Biological recognition element	Measurement technique	LOD[1]	Linear Range[1]	Non-target organisms used in selectivity	Ref.
Gold Substrates	Anti-*E. coli* (PA1-7213)[a]	EIS	2	$10 - 10^4$	*S. Typhyrium*	[111]
rGO paper/Gold NPs	Anti-*E. coli* O157:H7[b]	EIS	1.5×10^2	$10^2 - 10^7$	*E. coli DH5α; S. aureus; L. monocytogenes*	[112]
Gold Substrate	Anti-*E. coli* O157:H7[c]	EIS	10^2	$300 - 10^5$	*E. coli DH5α; E. coli K12; S. aureus*	[113]
Gold Substrate/Polyaniline	Anti-*E. coli* O157:H7[d]	EIS	10^2	$10^2 - 10^7$	*S. Typhyrium; E. coli BL 21*	[114]
Gold Screen Printed Electrodes	Thiolated anti-*E. coli* (CEC 515)	EIS	3.3	$5 - 10^8$	*S. choleraesuis; S. aureus*	[115]
Screen Printed Eelectrodes/rGO/GoldNPs	anti-*E. coli* O157:H7[e]	EIS	1.5×10^3	$1.5 \times (10^3 - 10^7)$	*E. coli DH 5α; S. aureus; L. monocytogenes*	[116]
SiO₂/graphene/PASE	anti-*E. coli* O157:H7	EIS (non-faradaic)	10	$10 - 10^7$	*E. coli DH5α*	[117]
rGO/Al₂O₃/Gold NPs	Anti-*E. coli* O/K[c]	FET	10^3	$10^3 - 10^5$	*S. Typhyrium; Streptoccocus pneumonia*	[118]
GCE/Chitosan/GO	ssDNA (*E. coli* O157:H7)	EIS	3.584×10^{-15} M	$10^{-14} - 10^{-8}$ M	-	[119]
Screen Printed Electrodes	T4 Bacteriophage (*E. coli* K12)	EIS	2×10^4	$10^2 - 10^8$	*S. Typhyrium*	[120]

rGO– reduced graphene oxide; **NPs** – nanoparticles; **PASE** - 1-pyrenebutanoic acid succinimidyl ester; **GCE** – glassy carbon electrodes; **GO** – graphene oxide; [1]**CFU/mL;** [a] Covalently bound using EDC/PFP/DIEA; [b] Linked through streptavidin-biotin interaction; [c] Covalently bound using EDC/NHS; [d] Linked through glutaraldehyde; [e] Immobilised through physical adsorption.

IV | Experimental Procedure

4.1   LIG electrodes production

The transducer element of the biosensor proposed in the present work is a laser-induced graphene (LIG) electrode. As mentioned before, LIG is the result of a photo-thermal effect of a laser beam on a polymer sheet, usually polyimide (PI).

In this thesis, the procedure takes advantage of a continuous CO_2 laser with a 10.6 μm wavelength for carbonisation of commercially available polyimide (PI) sheets, more specifically Kapton®. The process for LIG synthesis involves a scanning movement of the laser beam on the PI sheet setting plane. The scanning movement is controlled by two laser parameters: the speed of scanning, v_{laser} (mm/s), and the distance between lines of scanning, d (mm). Along with these, one can control the laser power output, P_{laser} ($\%P_{máx}$), and the distance between the laser head and the PI sheet, h (mm). Altogether, one can work these parameters to obtain LIG with the most suitable properties for the application intended. In **Figure 3.1**, a representative scheme of how LIG samples are produced is introduced.
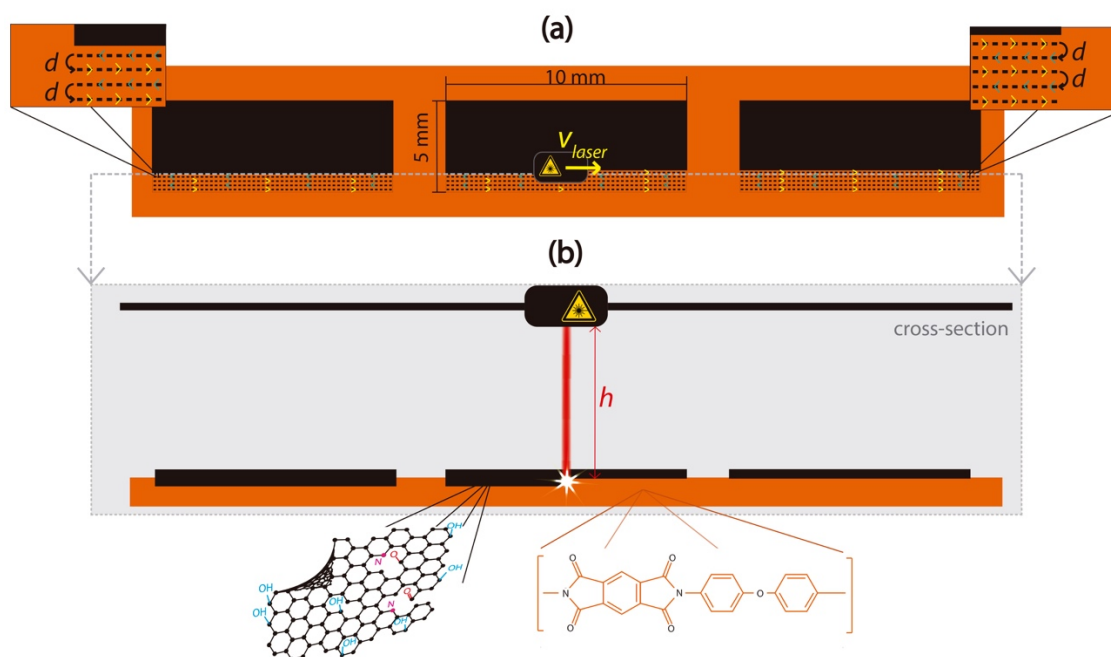
Figure 3.1: Scheme of LIG samples production, where (a) is the top view and (b) is the cross-section corresponding to the dashed line.

In this work, the synthesis of LIG was conducted on 127 μm thick Kapton® foil, using P_{laser}, d and h at constant values. P_{laser} was kept at 20% of maximum laser power, corresponding to ~9 W, d at 0.075 mm and h at 18 mm. These values were select based on a previous work of our group [121]. Thus, laser scan speed was the determinant variable studied, regarding the production of LIG with adequate electrochemical parameters. For that, five different v_{laser} were explored, 150, 200, 250, 300 and 350 mm/s. For each v_{laser}, three 10x5 mm^2 LIG samples were produced, as replicates (**Figure 3.2-a**).

Afterwards, each sample was submitted to a preparation protocol in order to obtain electrodes suitable for electrochemical measurements.

Primarily, all samples were washed by dipping them in deionised water and using magnetic stirring at 500 rpm for 5 minutes. Then, they were dried with a gentle N_2 flow.

Secondly, it was established an electrical contact to ensure simplicity when implemented into the electrochemical cell. For that, a silver-plated copper wire and silver ink (*Agar Scientific*) were used (**Figure 3.2**-b). To guarantee the maximum conductivity from the silver ink, at this phase the electrodes were allocated in an oven at a temperature between 70 and 80 °C for 30 minutes, following the instructions given by the supplier. Then, to fixate the electrochemical active area of the samples as well as to isolate the electrical contact from the electrolyte, one resorted to chemically inert Lacomit Varnish (*Agar Scientific*) (**Figure 3.2**-c).
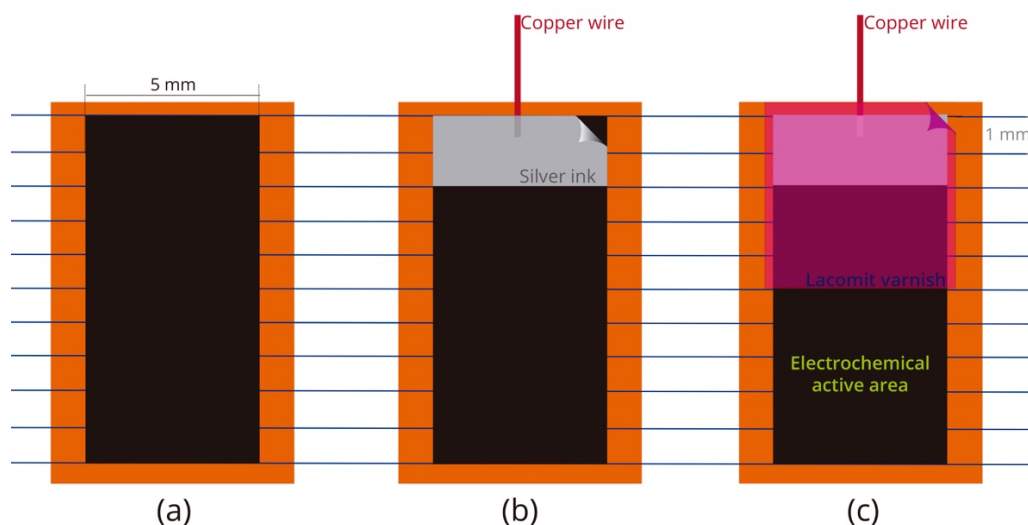
Figure 3.2: Scheme of the production of one LIG electrode for electrochemical measurements, in which (a) represents a single LIG sample, (b) the LIG sample after establishing the electrical contact using silver ink and a copper wire and (c) the final step of the electrode production with chemical isolation of the electrical contact and fixation of the electrochemical active area with the Lacomit varnish.

To understand the adequacy of the LIG electrodes towards electrochemical biosensing, one explored the heterogeneous rate transfer constant, $k^0 (cm \cdot s^{-1})$, the effective electroactive area, $A_{eff} (cm^2)$, and the capacitance per unit area, $\gamma_{dl} (F \cdot cm^2)$. For the determination of these values, each electrode was submitted to electrochemical measurements, cyclic voltammetry (CV) and chronocoulometry (CC) techniques. These measurements were performed using a Versastat3 electrochemical station (*Princeton Applied Research*) and a three-electrode configuration set up, where LIG was the working electrode (WE), Ag/AgCl (1 M KCl) (CHI111, *CH Instruments, Inc*) the reference electrode (RE) and a Pt wire the counter electrode (CE). The supporting electrolyte comprised 1mM of $K_4[Fe(CN)_6]$ (*Merck*) as the active redox specie dissolved in a 10 mM phosphate buffer saline solution (PBS, pH=7.4, from *Fisher Bioreagent*). In **Figure 3.3**, it is presented a representative scheme of the electrochemical cell used throughout the measurements. Further, the measurements were performed at low area-volume ratio conditions, since a 0.25 cm^2 working electrode area was measured in a 50 mL electrolyte solution. Prior to any electrochemical assessments, the electrolyte solution was bubbled with a N_2 flow, for 30 min. Throughout the discussion of the results (section 5.1), it will be explained the analysis employed to determine k^0, A_{eff} and γ_{dl}.
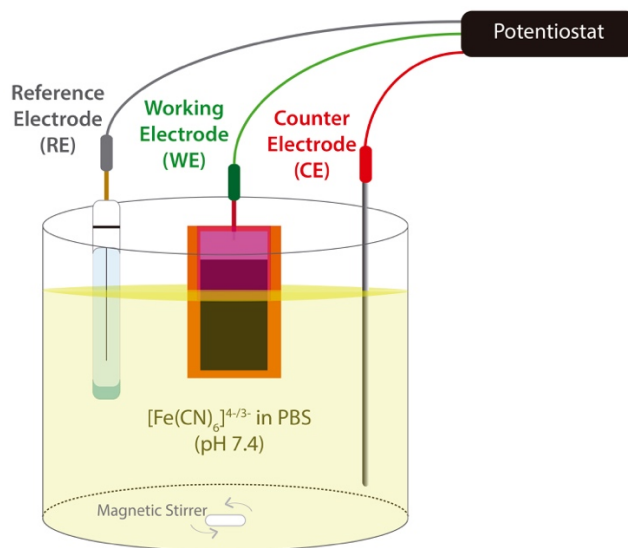
Figure 3.3: Schematic representation of the electrochemical cell.

Simultaneously, further characterisation was conducted, regarding the 5 laser scan speeds. So, for each v_{laser}, a representative electrode was characterised by Raman spectroscopy and scanning electron microscopy (SEM). The former was conducted on a Jobin Yvon HR800 instrument (Horiba, Japan), using backscattering configuration, with a 600 lines/mm grating and a He-Cd laser (Kimmon Japan) with a wavelength of 442 nm. To focus the laser onto the samples and to collect the backscattered Raman radiation, a 50x objective was used. The detection of such radiation was performed by a Peltier cooled (223 K) CCD sensor and the spectrometer was used in the confocal mode, with the iris set to 300 μm. The SEM imaging was accomplished using a TESCAN Vega3 SB instrument, in secondary electron mode. Further, after choosing the most fitted v_{laser}, a compositional characterisation was operated on the correspondent electrode by X-ray photoelectron spectroscopy (XPS). The XPS spectra were acquired in TEMA, University of Aveiro, using an Ultra High Vacuum (UHV) system with a base pressure of 2×10^{-10} mbar. The system comprises a monochromatic AlKα (1486.74 eV) X-ray source, a hemispherical electron energy analyser (SPECS Phoibos 150) and a delay-line detector. The spectra were recorded at normal emission take-off angle and with a pass-energy of 20 eV, providing an overall instrumental peak broadening of 0.5 eV.

4.2 Impedimetric Biosensor production

After choosing the best laser scan speed to produce the LIG electrochemical electrodes, it was required to plan and test a complete functionalisation of the electrode in order to detect the *E. coli*.

It was previously chosen that the biological recognition element of this biosensor would be an antibody, in this case *E. coli* serotype O/K Polyclonal Antiboby from *Thermo Fisher Scientific*. In order to immobilise the antibody correctly, meaning that the surface of the electrode is covalently bound to the antibody through its heavy chain, it is necessary to have an amine-terminated surface. So, following some functionalisation protocols contempling carbon-based biosensors [122], [123], it was decided to use the (3-aminopropyl)triethoxysilane (APTES, from *Merck*) as the ligand between the LIG surface and the antibody. Further, to ensure that after the silanization occurs, the amine groups are the ones available on the surface, it was required the presence of hydroxyl groups on the LIG surface. Hence, a four steps functionalisation was proposed and studied: surface hydroxylation,

APTES silanization, antibody immobilisation and passivation using bovine serum albumin (BSA). The latter is required to eliminate possible analyte and electrolyte adsorptions on the free (non-functionalised) electrode surface.

Initially, it was unclear the amount and distribution of hydroxyl groups on LIG's surface, so the need of a hydroxylation step was explored. Particularly, it was intended to explore the effect of performing this step, upon APTES functionalisation.

The hydroxylation was carried out via Fenton reaction, which is promoted by Fe(II) and H_2O_2 generating hydroxyl radicals (eq. 3.1) that attacks the graphene structure and provides hydroxylated LIG.

$$Fe^{2+} + H_2O_2 \longrightarrow Fe^{3+} + OH^. + OH^- \qquad \text{(eq. 3.1)}$$
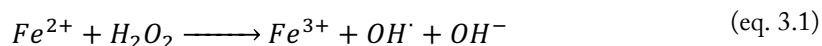
The Fenton reaction solution was prepared by slowly adding 103 mg of $FeSO_4 \cdot 7H_2O$ (*Panreac Aplichem*) to a continuously stirred aqueous solution of H_2O_2 (16 mL of H_2O_2 (30% v/v) diluted in 44 mL of deionised water). Before adding the electrodes, a 15 min wait secured less violent bubbling of the reaction and more stable pH (~4) and temperature (25 °C). Then, the active area of the electrodes was dipped in the stirred solution for 1h. The stop mechanism relied on dipping the active area of the electrodes on stirred DI water for 5 minutes followed by drying it with a gentle N_2 flow. To study the impact of the hydroxylation, three electrodes were submitted to electrochemical characterisation (determination of k^0, A_{eff} and γ_{dl}), to Raman spectroscopy and, also to XPS analysis.

Secondly, to acquire a amine surface termination, APTES silanization was carried out through immersing the electrodes on APTES (0.1, 1 and 10 %) dissolved in ethanol:H_2O (7:3 v/v) during 1 h. Afterwards, the electrodes were rinsed with DI water, dried with a gentle N_2 flow and soft baked at 120 °C for 20 minutes. This functionalisation was explored using XPS, along with the hydroxylation analysis, and later with EIS and CV electrochemical approaches to evaluate the concentration impact on it.

Once the electrode was amine-terminated (**Figure 3.4**-b), it enabled the anti-*E. coli* covalent immobilisation. For that, one resorted to *N*-(3-dimethylaminopropyl)-*N'*-ethylcarbodiimide hydrochlorine (EDC, *Sigma-Aldrich*) and *N*-hydroxysuccinimide (NHS, from *Sigma-Aldrich,* 98%), guaranteeing the covalent bond between the amine groups and the carboxylic groups on heavy chains of the anti-*E. coli*. The mixture consisted on 50 μL of anti-*E. coli* (1 mg/mL), 25 μL of NHS (0.2 M) and 25 μL of EDC (0.5 M). Here, a drop (50 μL) of this mixture was placed on the electrode active area during 2 hours (**Figure 3.4**-c). Then the electrodes were rinsed with PBS and dried with a gentle N_2 flow.

Finally, the passivation of the electrode was carried out using a 1% BSA (Standard Grade Powder from Fisher Bioreagents) solution. For that, the electrode was exposed to a 50 μL drop for 30 minutes (**Figure 3.4**-d), then rinsed with PBS and dried with a gentle N_2 flow. During both antibody and BSA functionalisation, the electrodes were kept at 4 °C. The same was done, while resting until electrochemical measurements and /or bacteria immobilisation protocol.

All the functionalisation steps were characterised through EIS and CV measurements. The experimental setup was equivalent to the one used in electrochemical techniques, in section 4.1. Nonetheless, for both techniques the electrolyte consisted on a 1 mM of $K_4[Fe(CN)_6]$ and 1 mM of $K_3[Fe(CN)_6]$ in 10 mM PBS solution. During EIS measurements, the solution was kept under stirring (500 rpm). Since this technique allows to capture responses from electrochemical phenomena occurring both on the WE interface and on the bulk solution, it was verified that in this case, a

natural convection phenomena raised on the electrolyte. The latter disturbed the system resulting on non-stable EIS response through time. To solve this problem, it was suggested stirring the bulk solution, provoking a forced convection on the system and, consequently, stabilizing the EIS response [63]. Moreover, the EIS measurements were performed using a 5 mV AC perturbation in the $1\text{-}10^4$ Hz range upon the OCP DC bias (~0.19 V vs Ag/AgCl (1M)). On the other hand, during CV measurements, the solution was not stirred. These were performed applying a DC potential, from -0.2 to 0.6 V and backwards, with a 50 mV/s scan speed.

The results from EIS and CV measurements are presented and discussed in section 5.2. From this discussion, a complete functionalisation protocol was chosen to embody the impedimetric biosensor prototype to be tested for *E. coli* presence and it is presented in **Figure 3.4**.
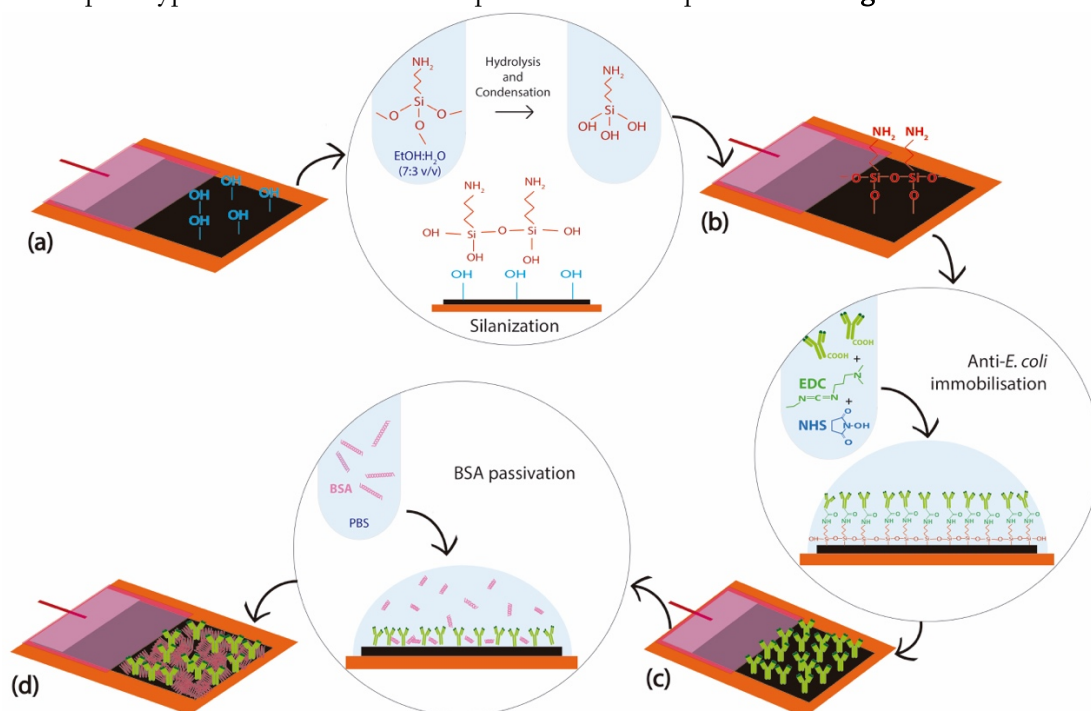
Figure 3.4: Representative scheme of the functionalisation protocol for production of the impedimetric biosensor, in which (a) is the LIG electrode, (b) the APTES-functionalised electrode, (c) the electrode with the immobilised anti-*E. coli* and (d) the passivated electrode.

4.3   *E. coli* immobilisation and tests
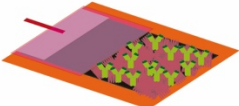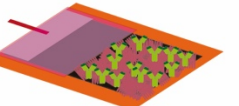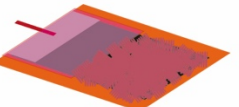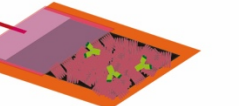
Having the functionalisation protocol studied, the final step of this work was to test the fully functionalised electrodes towards different *E. coli* concentrations in order to prove the concept of biosensor.

To start, the *E. coli* strain ECR1, from a private collection of the Microbiology group in University of Aveiro (http://biomicrolab.web.ua.pt/) [124], was inoculated in Luria Bertani (LB) medium and incubated for 16h at 37 ˚C. In order to establish the several *E. coli* concentrations to test, optical density was measured at 600 nm. In fact, this measurement provides an estimation number of *E. coli* cells in the solution (1 OD at 600 nm approximately corresponds to 8×10^8 cells/mL), enabling to proceed with the biosensor tests using fresh cells. However, the result was confirmed later through plate counting technique as protocol. Then, after addressing the *E. coli* concentration of the inoculum, the latter was diluted in PBS, resulting in 7 concentrations: 5, 10,

10^2, 10^3, 10^4, 10^5, 10^6 CFU/mL. Cell numbers estimations were confirmed through plate counting. For this, the bacterial culture was serially diluted in PBS and plated in triplicate on LA (LB supplemented with agar at 1.5%). After 16h of incubation at 37 °C, the colony forming units were enumerated. The exact same procedure was performed for *Shewanella* strain IR24 [125], the bacteria used to prove selectivity. Both *E. coli* and *Shewanella* dilutions were kept at ~4 °C before and during the biosensor tests.

Concerning the biosensor test, besides the fully functionalised electrodes, a set of electrodes was prepared with the intent of disclose false-positive results. Hence, the set of electrodes tested is presented in **Table 3.1**, where for each test the corresponding target bacteria are mentioned.

Table 3.1: Set of tests performed, including the controls, and the designated target bacteria tested.

	EIS Tests	Target Bacteria
Biosensor (Fully functionalized)		*E. coli* (ECR 1)
Selectivity (Fully functionalized)		*Shewanella*
Control (No anti- *E. coli*)		*E. coli* (ECR 1)
Control (No EDC/NHS)		*E. coli* (ECR 1)

Anti-*E.coli* ; BSA

Each electrode was tested for the 7 concentrations of bacteria prepared, in ascending order. That said, the electrodes were initially dipped in the 5 CFU/mL solution for 45 min, to assure enough time for bacteria immobilisation. Afterwards, the electrodes were rinsed with PBS to remove non-bounded material, such as bacteria and culture medium nutrients, and gently dried with a N_2 flow. Then, to obtain the test response, each electrode was submitted to one EIS measurement, under the same conditions used in the section before. Finally, the electrodes were rinsed with PBS and dried with a gentle N_2 flow. Consequently, this procedure was repeated for each concentration and the results obtained are presented and discussed in section 5.3.

V |Results and Discussion

5.1   LIG electrodes Characterisation

The aim of this thesis was to develop a LIG impedimetric biosensor for *E. coli* detection. So, to adequately accomplish it, the starting point of this work settled on the production and characterisation of the LIG samples, using as starting material a polyimide (PI) foil. More specifically, attempting to evaluate the influence of the laser scan speed (v_{laser}) on morphological characteristics and electrochemical properties of LIG. With respect to that, samples for each of the five v_{laser} (150, 200, 250, 300 and 350 mm/s) were studied through scanning electron microscopy (SEM) and Raman spectroscopy and by electrochemical measurements.

In **Figure 4.1**, **SEM images** acquired for each v_{laser} are presented. Recalling the laser process described in section 4.1, the samples arise from linear spaced passages of the laser beam onto the Kapton foil. In fact, one can notice well these passages for the lower v_{laser} (**Figure 4.1**-a and b) which can be interpreted as the formation of valley- and hill-like morphologies. These morphologies are inherent to the effect of the laser beam on the PI, including the temperature diffusion, as depicted in the work developed by Sida et al. [106], where the influence of laser power on these morphologies was studied. In **Figure 4.1**, one can see the impact of the v_{laser}, which can be interpreted as the time that the laser spot interacts with PI, on these formations and on the porous distribution. Indeed, with increasing laser scan speed, one observes that the uneven morphology turns less accentuated and the number of porous tends to rise. These morphologies are related to laser spot overlapping on the nearby regions of the LIG structure, meaning new temperature gradients responsible for rearrangements of the structure, emphasizing these formations and the number of porous. A magnified view of these surfaces can be seen in **Figure 4.2** that enables to observe in detail the typical surface and the porous structure inherent to LIG samples.
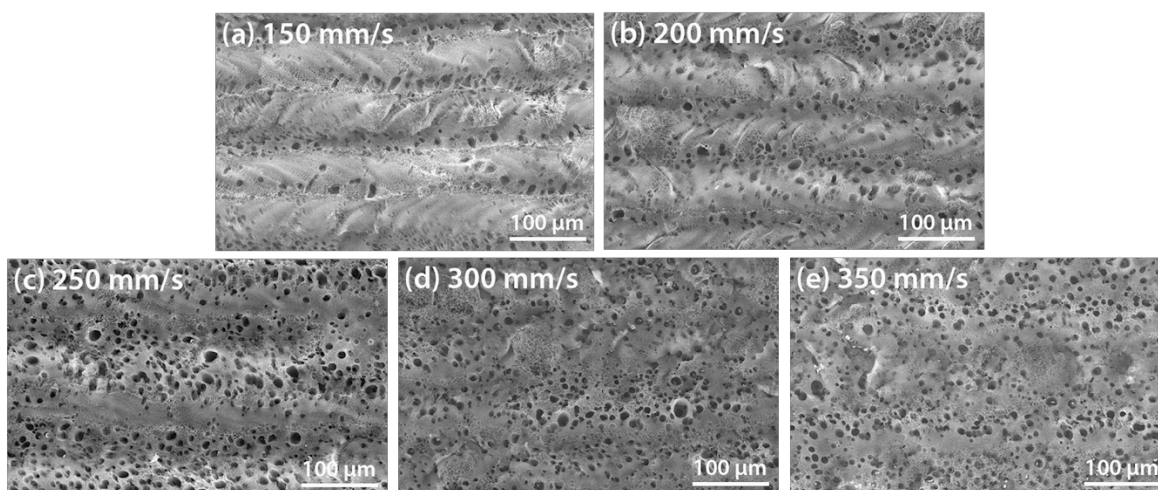
Figure 4.1: SEM images of the LIG samples produced by laser interaction with the Kapton® foil using the five vlaser, (a) 150 mm/s, (b) 200 mm/s, (c) 250 mm/s, (d) 300 mm/s and (e) 350 mm/s.
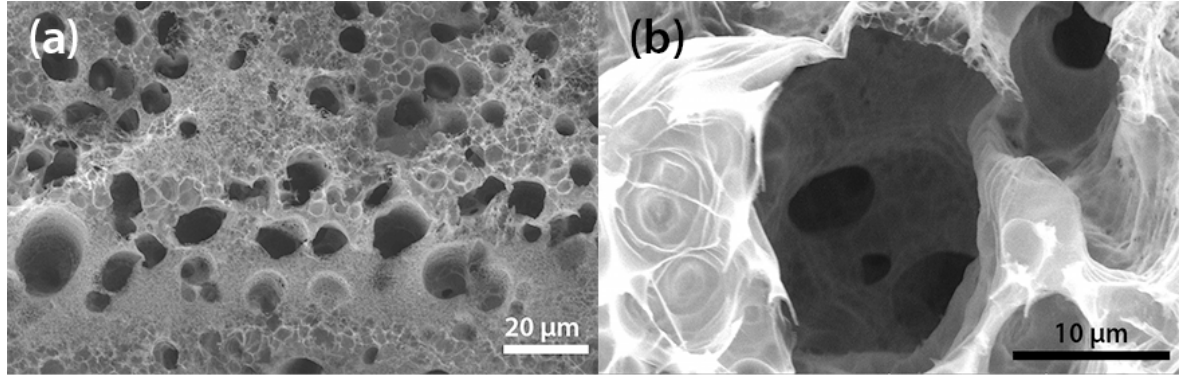
Figure 4.2: Magnified SEM images of the LIG sample produced with 300 mm/s. In (a), it is highlighted the surface morphology and the porous distribution. In (b), one focus on a porous structure.

In order to structurally characterise the LIG samples processed under different v_{laser}, Raman spectroscopy was performed. This is a well-established characterisation technique for carbon allotropes, providing information about structural and electronic properties, particularly in graphene samples, in a non-destructive way [126]. For each sample, five random sites were chosen for acquisition of spectra. Also, within these five sites, an effort was made to obtain spectra for valley- and hill-like localisations. For every v_{laser}, the spectra obtained are very similar, even between valley- and hill-like sites, with exception for the LIG sample produced with 250 mm/s, where the presence of the D' band is slightly perceptive. Thus, in **Figure 4.3**, the Raman spectra of LIG samples are presented, distinguishing the LIG produced with 250 mm/s (**Figure 4.3**-b). In both spectra, one can identify the three most prominent bands, the G, the D and the 2D, typical of graphene-based materials.
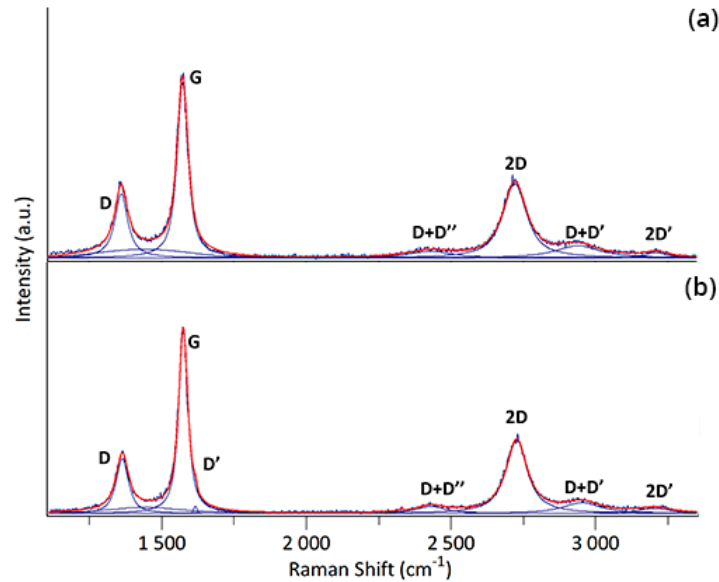
Figure 4.3: Raman spectra of LIG samples. (a) Representative Raman spectrum for LIG produced with 150, 200, 300 and 350 mm/s. (b) Raman spectrum obtained for LIG produced with 250 mm/s.

The most intense band, appearing at ~1573 cm^{-1}, is the G band and is ascribed to one-phonon scattering of the stretching mode of sp^2 carbon bonds [127]. Moreover, the presence of the D band, at ~1358 cm^{-1}, indicates the existence of defects on graphene structure. This band is originated by double-resonance mechanism comprising the scattering of one-phonon of the breathing mode of

defective aromatic rings, which present an additional scattering at the defect sites [126]. The ratio between intensities of the D and G bands, I_D/I_G, enables the evaluation of the defect density on the graphene-based material. In contrast, the 2D band, which is the D band overtone, does not require defects for its activation since it rises from the scattering of two phonons, with symmetric momenta, of the breathing mode of (perfect) aromatic rings. In this case, the double-resonance process associates the phonons to the electronic bands of graphene [126]. So, for single-layer graphene, the 2D is a sharp peak with the highest intensity of the spectrum. Increasing the number of graphene layers the peak will broaden and its intensity decreases. The interaction between graphene layers causes a splitting of the electronic bands and, consequently, splitting the 2D signal [126], [128]. Nonetheless, the splitting of this peak occurs for samples where the graphene layers follow Bernal stacking. For disordered multilayer graphene samples, as incommensurable graphene, a much less intense single 2D peak is presented [126], [129]. Hence, the shape and intensity of this band enables one to report about the number of graphene layers and, simultaneously, to state about its stacking. Usually, this information is integrated in the ratio between intensities of the 2D and G bands, I_{2D}/I_G, identifying the number of graphene layers, for samples up to five layers. In **Figure 4.3**, the 2D appears at ~2719 cm^{-1} presenting a broad single peak shape with lower intensity than the G band. Additionally, one can spot other bands in **Figure 4.3**, such as D', only perceptive in **Figure 4.3**-(b), 2D', D+D" and D+D'. Similarly to the D band, D' is generated from double-resonance of one-phonon process also activated by the presence of defects, but it was explored to outstands upon vacancy-type defects [130]. In **Figure 4.3**, D' appears at ~1620 cm^{-1} and its overtone, 2D', at ~3203 cm^{-1}. As 2D band, 2D' involves two-phonon scattering, not requiring defects for its appearance on the Raman spectrum. Besides D and D' bands, the presence of defects also gives rise to two-phonon processes assisted by electron-defect scattering, originating combination bands, such as D+D" and D+D' [126]. In **Figure 4.3**, these appear at ~2429 and ~2949 cm^{-1}, respectively. Further, in order to have a good fitting of the obtained spectra, it was necessary to account with the broad band assigned to amorphous carbon at ~1440 cm^{-1} [126]. Lastly, one can notice a small peak at ~2327 cm^{-1} ascribed to atmospheric nitrogen in the laser focus region [131].

To evaluate the differences between the LIG produced by the different v_{laser}, both I_D/I_G and I_{2D}/I_G were determined and are introduced in **Table 4.1**. These values were established by the mean of the ratios for each of the five sites analysed, for each v_{laser}.

Table 4.1: Intensity ratios I_D/I_G and I_{2D}/I_G for each laser scan speed.

	150 mm/s	200 mm/s	250 mm/s	300 mm/s	350 mm/s
I_D/I_G	0.30 ± 0.04	0.33 ± 0.04	0.29 ± 0.08	0.37 ± 0.07	0.36 ± 0.07
I_{2D}/I_G	0.42 ± 0.03	0.43 ± 0.02	0.40 ± 0.04	0.43 ± 0.03	0.41 ± 0.03

Analysing **Table 4.1**, it is not noticeable significant differences between LIG produced by the five v_{laser}. Thus, one concludes that the laser scan speed, for these five speeds, does not influence significantly the density of defects as well as the orientation and number of layers of LIG. Actually, the unique difference noted was the manifest of a small D' band for the LIG produced with 250 mm/s. Accordingly to the previous results, one can state that LIG samples are in fact defective graphene, as it is an aspired result for the main aim of this work. As mentioned in section 2.3, the presence of defects raises the kinetics in electrochemical systems, conceding great sensibility towards impedimetric measurements.

Envisioning the **electrochemical characterisation**, LIG electrodes were prepared as described in section 4.1, in which electrical contacts were established, using a copper wire and silver ink, and the electrochemical area of each electrode was fixed. This constituted an important step, since the aim of such characterisation was to determine and compare the values of the heterogeneous rate transfer constant (k^0), the effective electroactive area (A_{eff}) and the capacitance per unit area (γ_{dl}) for each v_{laser}, which will be explained in the following paragraphs. The electrolyte used to accomplish the voltammetric and chronocoulometric measurements required to determine the k^0 and A_{eff} values, respectively, was a 1mM $[Fe(CN)_6]^{4-}$ in phosphate buffer saline, PBS (10mM), solution. To determine the γ_{dl}, the electrolyte consisted only on PBS (10mM) solution, without resorting to any redox species. The use of 10 mM PBS solution as supporting electrolyte is crucial to settle the pH and ionic strength conditions of the electrochemical measurements. Consequently, establishing the oxidation-reduction potential and uniformity of ionic strength throughout the solution, maintaining the diffusion layer sufficiently thick (semi-infinite) in comparison to the double-layer on the electrodes' surface, for mass transport purposes [63], [132].

The heterogeneous charge transfer rate constant, k^0, describes the kinetics at electrode-electrolyte interface. Conveniently, this rate is intimately related to the charge-transfer resistance in faradaic impedimetric biosensors. Hence, the determination of this parameter enables to evaluate the suitability of LIG in this type of electrochemical sensing technology. Further, establishing the electrochemical active area, A_{eff}, allows to assess the effective area of the electrodes for which faradaic processes take place. Finally, the capacitance per unit area, γ_{dl}, concedes an estimation of the double-layer capacitance, which turns useful when fitting the Nyquist plots to the equivalent circuit.

Particularly, k^0 enables to understand if the charge-transfer process is sufficiently fast in comparison with the rate for which diffusive processes take place. Consequently, it is also a good indicator of the reversibility of the system, clarifying the aptitude of the electrodes to work on reversible, quasi-reversible or irreversible regimes [63]. To determine k^0, one resorted to cyclic voltammetry (CV) at different scan rates (100, 150, 200, 250, 300, 350, 400, 450, 500 and 600 mV/s). These were performed by applying a DC potential from -0.2 to 0.6 V. An example of the voltammograms obtained is introduced in **Figure 4.4**-(a).
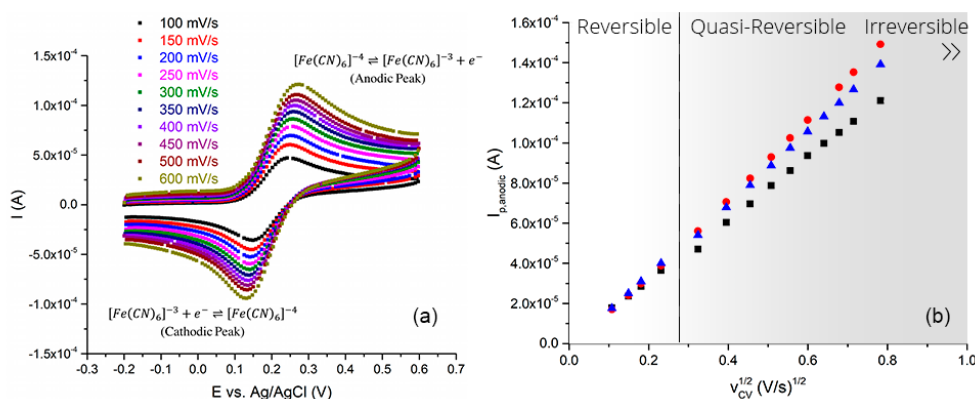
Figure 4.4: (a) Obtained voltammograms using ten different scan rates on one of the electrodes produced with 250 mm/s laser scan speed, measurements using $[Fe(CN)_6]^{4-}$ in PBS. (b) Anodic peak current behaviour regarding voltammetric scan rate. The three symbols represent three electrodes produced with same v_{laser}.

The voltammograms consistently spot two peaks, the anodic and the cathodic peaks, corresponding to the oxidation and reduction of the redox species ($[Fe(CN)_6]^{4-/3-}$), respectively. Further, increasing scan rate, an evolution of the current response and respective potential is

noticeable. For fact, the difference between the anodic and cathodic peaks potential, $\Delta E_p = E_{p_{anodic}} - E_{p_{cathodic}}$, as well as the current ratio, $\frac{i_{p_{anodic}}}{i_{p_{cathodic}}}$, evolve regarding the scan rate, usually towards irreversibility for higher scan rates. In the ideal case, i.e. for reversible systems, the peak current ($i_{p_{anodic}}$) is described by the Randles-Sevcik equation [63],

$$i_p = (2.69 \times 10^5) n^{3/2} A C (Dv)^{1/2} \qquad \text{(eq. 4.1)}$$

where n is the number of electrons involved in the redox event, A (cm^2) is the electroactive area of the electrode, C (mol/cm^3) is the reduced electroactive species concentration, D (6.67×10^{-6} cm^{2}s for $[Fe(CN)_6]^{4-/3-}$) is its diffusion coefficient and v (V/s) the applied scan rate. Constricting n, A, C and D to invariable behaviour, one observes the peak current dependence on the square root of the scan rate (**Figure 4.4**-b). However, the ΔE_p is constant for this working regime, $\Delta E_p \approx 57\ mV/n$, meaning that the heterogeneous electron transfer rate is sufficiently fast, so that the diffusion, mass transport of the species to the electrode, governs the net charge reactions completely [63], [133]. In fact, the shift of ΔE_p is only detected when the system starts to move away from reversibility (from v= 0.10 V/s, inclusive). In **Figure 4.4**-(a), this shift is perceived and, for all the scan rates used, the ΔE_p takes values between 57 and 230 mV, guaranteeing a quasi-reversible working regime. It is important to highlight that this was verified for the samples produced with the five v_{laser}. A very common method for determining the k^0 is the Nicholson method [63]. The latter applies to quasi-reversible systems and allows to connect the evolution of ΔE_p against the scan rate with a dimensionless parameter, Ψ. Subsequently, one can determine k^0 through the following equation

$$\Psi = \frac{k^0}{\left(\frac{n\pi FDv}{RT}\right)^{\frac{1}{2}}} \qquad \text{(eq. 4.2)}$$

in which F is the Faraday constant (96485.33 C/mol), R the universal gas constant (8.314 J/Kmol) and T the temperature (K). Nicholson determined very exact and precise values of Ψ for certain ΔE_p. By means of fitting a proper function to this well-known set of points, one can then determine the Ψ for every ΔE_p obtained for each scan rate (**Figure 4.5**-a). Finally, the linearly proportionality between the Ψ and the $v^{-\frac{1}{2}}$ (**Figure 4.5**-b) concedes the assessment to the k^0 of the electrode.
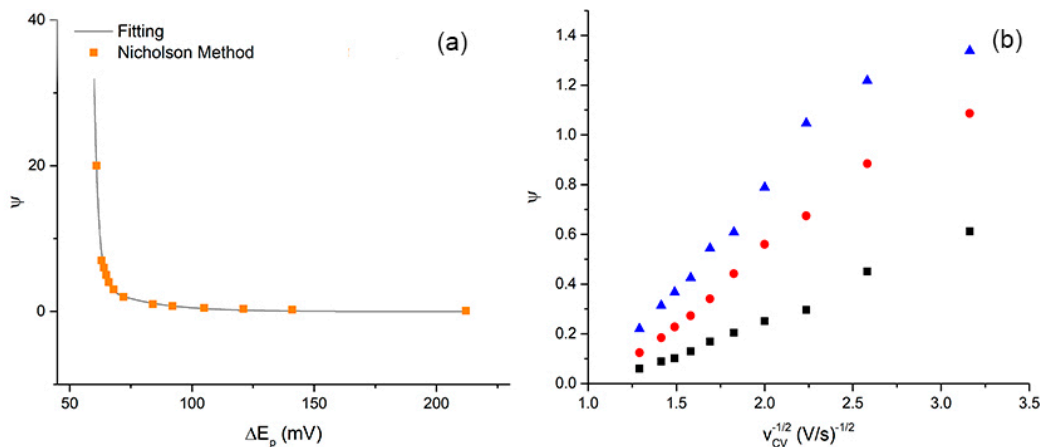

Figure 4.5: (a) Fitting function (black line) used to determine the Ψ parameter towards ΔE_p and the Nicholson method set of points (orange squares) that originated the same. (b) Ψ parameter linear dependence concerning $v^{-\frac{1}{2}}$ for the three electrodes produced with 250 mm/s, as an example.

This analysis was performed on three electrodes for each of the five v_{laser}, assuring reproducibility on the measurement. In **Figure 4.6**, it is introduced the k^0 for each v_{laser}, which values are the means of the k^0 obtained for each of the three electrodes.
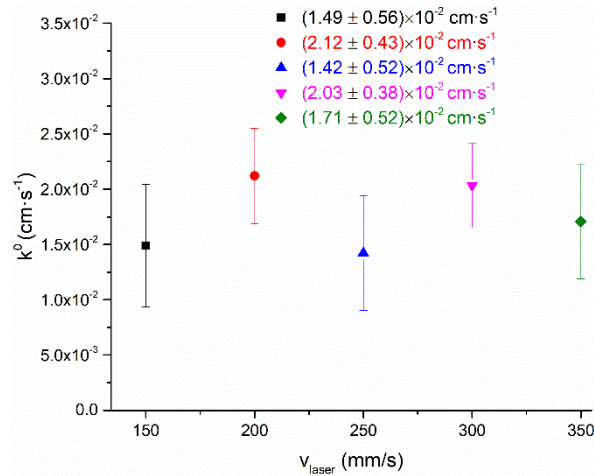
Figure 4.6: Heterogeneous charge transfer rate constant, k^0, for each laser scan speed, v_{laser}.

It is noteworthy that the heterogeneous charge transfer rate constant was very similar for all the LIG produced, presenting values in the order of 10^{-2} cm/s. In comparison with other carbon-based electrodes of reference, such as boron-doped diamond (BDD), bare glassy carbon (GC), graphite and carbon nanotubes (CNTs), among others, the presented LIG electrodes exhibit an excellent heterogeneous electron transfer rate constant. In **Table 4.2**, it is presented a brief list of carbon-based electrodes and the correspondent k^0, using $[Fe(CN)_6]^{3-}$ or $[Fe(CN)_6]^{4-}$ in PBS or potassium chloride (KCl) solution.

Table 4.2: List of some relevant carbon-based electrodes and respective k0 values, using $[Fe(CN)_6]^{3-}$ or $[Fe(CN)_6]^{4-}$ in PBS or potassium chloride (KCl) solution.

Electrode	k^0 (cm/s)	Ref.	Electrode	k^0 (cm/s)	Ref.
GC	3.22×10^{-5}		BDD	$\sim 10^{-2}$	[135]
CNTs	5.09×10^{-6}	[134]	GC	2.9×10^{-2}	[136]
Graphite	1.76×10^{-4}		rGS[c]	4.9×10^{-2}	
NC[a]	3.30×10^{-3}		MG[d]	1.2×10^{-3}	[137]
FGS-ML[b]	5×10^{-2}	[138]	MWCNT	5×10^{-1}	[139]

[a]Nanoporous Carbon; [b]Functionalised graphene sheets monolayer; [c]Reduced graphene sheets; [d]Monolayer graphene.

To determine the A_{eff}, instead of using the Randles-Sevcik equation, which can only be applied in reversible systems, it is preferable to use a reversibility independent method that takes advantage of chronocoulometry (CC) technique. In this technique, a potential step, slightly over the oxidation potential, is applied to the system for a certain amount of time (0.1-2.0 s). Thus, guaranteeing the oxidation of the species for all the electroactive area of the electrode under a controlled-diffusion regime [63]. As the name of the technique indicates, one measures the amount of charge (coulometry) accumulated on the electrode's electroactive surface as a function of time (chrono) [140]. The time (t) dependence of the accumulated charge (Q_{acc}) is governed by the integral form of the Cottrel equation [63]

$$Q_{acc} = \frac{2nA_{eff}FC(Dt)^{\frac{1}{2}}}{\pi^{\frac{1}{2}}} + constant \qquad \text{(eq. 4.3)}$$

in which the constant is associated with the adsorbed species, defining the linear dependence of Q_{acc} towards $t^{\frac{1}{2}}$ and, subsequently, enabling the determination of the A_{eff}.

In this work, a complete chronocoulometry was performed. So, concerning the used supporting electrolyte ($[Fe(CN)_6]^{4-}$ in PBS), a 0.4 V potential step was applied, oxidizing the species, for 2 s followed by a 0 V potential step, reducing the product of the first step, for 2 s (**Figure 4.7**-a). To note that only the data related to oxidation of the species was further used for the analysis. Similarly to the k^0 analysis, three electrodes, for each v_{laser}, were submitted to this technique for three times each. Moreover, the electroactive area was analysed for three electrolyte concentrations, 1, 2 and 5 mM of $[Fe(CN)_6]^{-4}$.
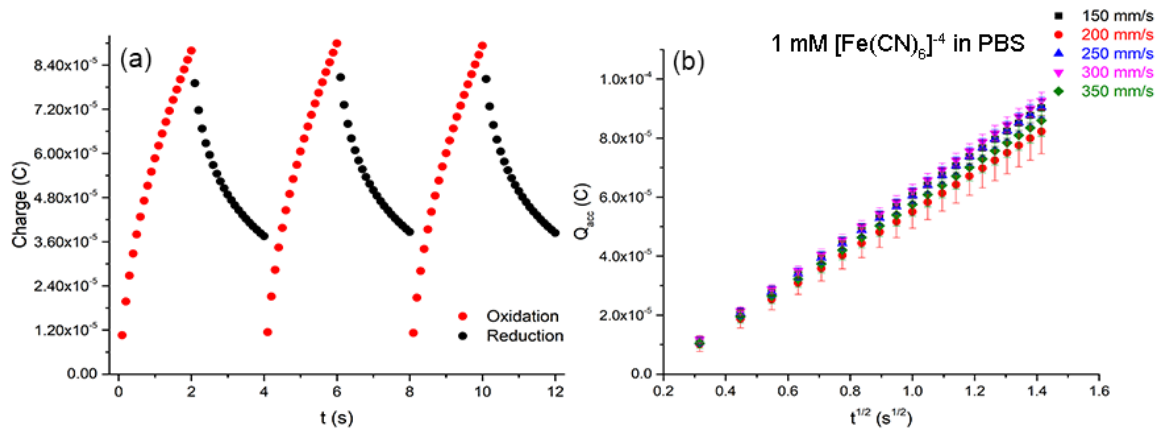
Figure 4.7: (a) Obtained chronocoulometric plot using one of the electrodes produced with v_{laser} = 250 mm/s, as an example. (b) Plot of the accumulated charge, Q_{acc}, against $t^{\frac{1}{2}}$ obtained for the five v_{laser} using as electrolyte 1 mM $K_4[Fe(CN)_6]$ in PBS (10 mM, pH= 7.4).

The linearized charge response for 1mM $K_4[Fe(CN)_6]$ electrolyte is introduced in **Figure 4.7**-(b), as an example. In fact, the charge response obtained for the three concentrations followed the linear proportionality described by (eq. 4.3). So, as expected, the A_{eff}, for each v_{laser}, presented the same values for the three electrolyte concentrations. Accordingly, in **Figure 4.8** are depicted, as an example, the values determined using 1mM $K_4[Fe(CN)_6]$ electrolyte. The values obtained indicate that, for the five v_{laser}, the effective electroactive area is very close to the geometric area (0.25 cm^2) of the electrodes. As a matter of fact, it was expected a significant difference between the effective and the geometric area, since LIG detains a prominent porous structure, shown in **Figure 4.1**. It was thought that the similarity between the effective and geometric electroactive area was due to low wettability of the LIG electrodes, which could depress the porous structure potentiality to increase the effective electroactive area. So, in section 5.2, regarding the Fenton reaction results, the effect of increasing wettability on the effective electroactive area is discussed.
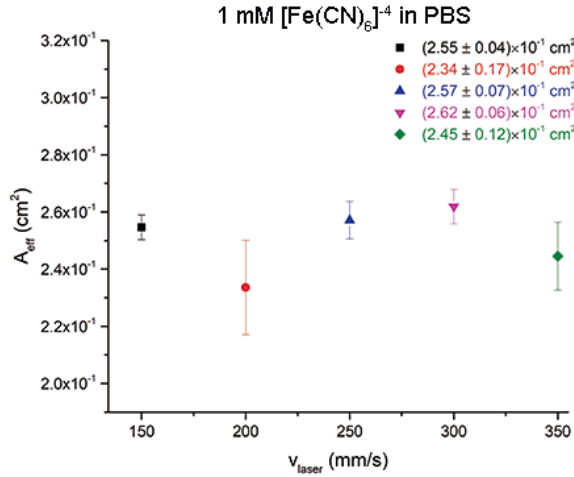
Figure 4.8: The effective electroactive area, A_{eff}, for each laser scan speed, v_{laser}, using the 1 mM $[Fe(CN)_6]^{4-}$ in PBS as electrolyte.

The analysis to determine the capacitance per unit area, γ_{dl}, starts similarly to the k^0, by applying cyclic voltammetry at different scan rates (5, 10, 20, 30, 50, 100, 250 and 500 mV/s), but using PBS without any redox species ($[Fe(CN)_6]^{3-/4-}$) as electrolyte (**Figure 4.9**-a). The applied DC potential range was the same as for the k^0 (from -0.2 to 0.6 V). In this analysis, the key point is to determine the current contribution of the double-layer, which contributes as background in faradaic processes analyses [63]. In **Figure 4.9**-(a), it is noticeable that the current response is not linearly constant from -0.2 to 0.6 V, implying some oxidation or adsorption reactions, mainly between -0.2 and 0.1 V. So, to ensure that the current response is strictly from the PBS, meaning from the double-layer capacitance, the value chosen was 0.2 V, which also is very close to the open-circuit potential (OCP) of the electrochemical cell, using $[Fe(CN)_6]^{-3/-4}$ in PBS as electrolyte.
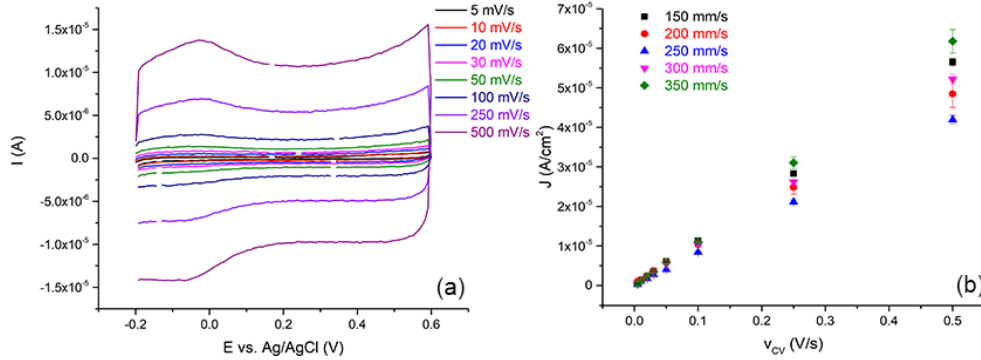
Figure 4.9: (a) Obtained voltammograms using eight different scan rates on one of the electrodes produced with 250 mm/s laser scan speed, using PBS as electrolyte. (b) Plot of the current density, J, against the scan rate, v_{CV}, obtained for the five v_{laser}.

Consequently, for each of the voltammograms, the current value, i, for 0.2 V potential was extracted. This value is used to determine the current density, J, by means of dividing it with the effective electroactive area, A_{eff}. As a consequence, J has a linear dependence on the applied scan rate defined by the following equation

$$J = \frac{i}{A_{eff}} = \gamma_{dl} v_{CV}$$

(eq. 4.4)

In **Figure 4.9**-(b), it is presented the current density linear dependence on the scan rate, for each of the v_{laser} and, in **Figure 4.10**, the γ_{dl} for each v_{laser} is shown. The values presented correspond to only one electrode per v_{laser}.
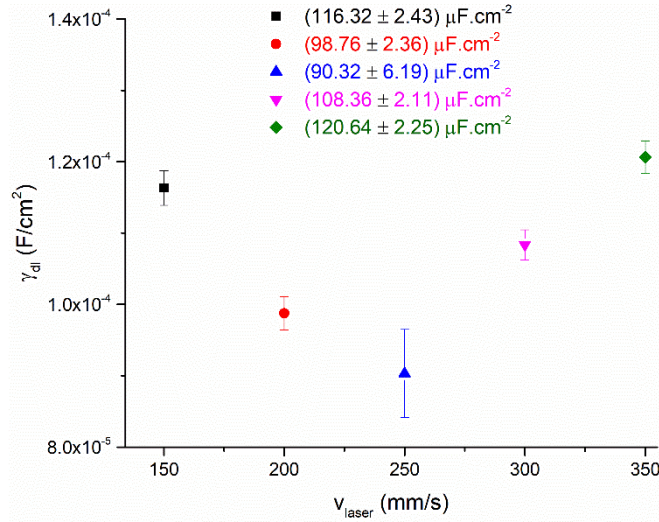
Figure 4.10: Capacitance per unit area, γ_{dl}, for each laser scan speed, v_{laser}.

In a pragmatic point a view, the main goal of this thesis is to use LIG electrodes as base of impedimetric biosensors, employing electrochemical impedance spectroscopy (EIS). Regarding the k^0 results, it was clarified the potentiality of LIG in faradaic biosensors. As explained in section 2.2, this type of biosensors comprehends both kinetics and diffusion processes, which can be interpreted by means of an equivalent circuit (**Figure 2.2**). Hence, it is required a limiting criterion so that the analysis can be done through the modified Randles circuit. That said, the R_{CT} values, which are intimately related with the k^0, should not be too high so that the charge transfer is dominated by the CPE branch. Therefore, there is a k^0 low-limit, ensuring that the latter situation does not occur and is set by the following condition

$$k_{lim}^0 \geq \frac{RTC_{dl}\omega}{F^2CA_{eff}} \qquad \text{(eq. 4.5)}$$

In which $\frac{C_{dl}}{A_{eff}} = \gamma_{dl}$ [63]. In fact, this condition clarifies that the γ_{dl} parameter should be kept low so that, upon EIS measurements and biosensing response, one can obtain measurable and distinguishable R_{CT} values, with good sensibility.

As a matter of fact, the characterisation of the LIG samples and electrodes, regarding the v_{laser}, have shown that for these laser scan speeds (150, 200, 250, 300 and 350 mm/s) the properties of the electrode do not differ significantly, resulting in very similar electrodes. Nonetheless, the LIG electrodes produced with 250 mm/s presented a lower γ_{dl}, insuring a more modest k^0 low-limit to proceed with functionalisation steps. Therefore, it seemed adequate to choose the sample produced with 250 mm/s to proceed with the functionalisation.

In this thesis, in order to attain a biosensor, the functionalisation of the electrodes comprised chemical modification of its surface through a series of chemical reactions, as specified in section 4.2. Since the main goal of this step was to covalently bound the antibody with the right orientation, it was imperative to have an amine-terminated surface. Therefore, according with the selected protocol, it was mandatory to have hydroxyl (OH) groups on the surface. Thus, the chosen LIG sample was analysed through **X-ray photon spectroscopy (XPS)**, in order to identify its surface functional groups.

In **Figure 4.11**, the C 1s (a) and O 1s (b) regions of the XPS spectrum are presented as well as the respective fitted peaks.
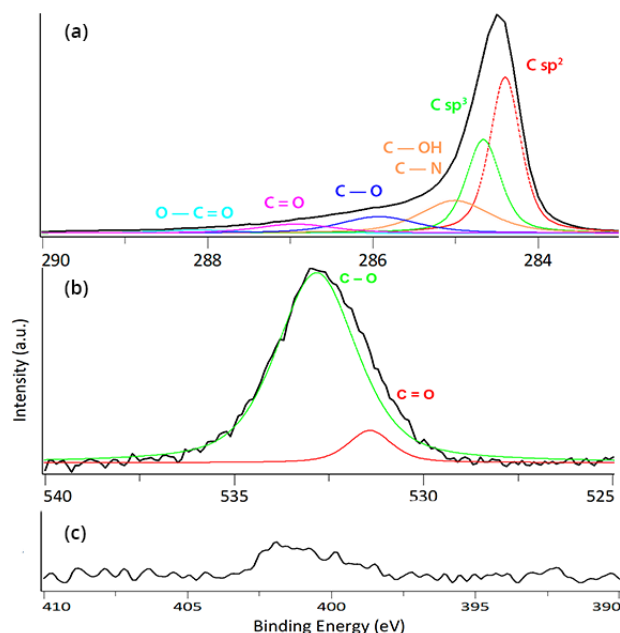
Figure 4.11: (a) C 1s, (b) O 1s and (c) N 1s regions of the XPS spectrum (black curves) of LIG produced with 250 mm/s. The corresponding fitted peaks are the coloured lines.

The C 1s spectrum is dominated by the two peaks at ~284.4 eV (red line) and ~284.7 eV (green line), corresponding to sp^2 (C=C) and sp^3 (C-C and C-H$_x$) bonding. The former has a greater contribution, which agrees with the Raman characterisation and confirms the graphitic nature of LIG [26], [94], [100], [141]–[145]. The presence of oxidised carbon is verified by the suppressed peaks at ~285.0 eV (yellow line), ~285.9 eV (dark blue line), ~286.9 eV (pink line) and ~288.1 eV (light blue line). The first, at ~285.0 eV, can be associated to the presence of hydroxyl groups (C-OH) and graphitic nitrogen (C-N) [92], [142]–[144]. Confronting this information with the O 1s and N 1s region of the spectrum, presenting the latter a non-defined contribution [100], one can conclude that this peak is mainly due to C-OH groups. The second peak, at ~285.9 eV, is assigned to epoxy and ether groups (C-O) [94], [141] and verified by the fitted peak at ~532.8 eV (green line) [26], [94], [146] in **Figure 4.11**-(b). Further, at ~287.9 eV (pink line) appears the small contribution of carbonyl groups (C=O) [144], [145], also confirmed in the O 1s region with the peak at ~531.4 eV (red line) [26], [94], [141], and at ~288.1 eV (light blue line) the highly suppressed peak related to carboxylic and ester groups (O-C=O) [142]. Therefore, in terms of surface's composition, the produced LIG exhibits very similar results to reduced graphene oxide (rGO) synthesised from graphene oxide (GO), mentioned in section 2.3, particularly by the presence of hydroxylated and oxidised carbon.

5.2 Functionalisation analysis

Having the LIG electrode characterised, the second milestone, in order to obtain an impedimetric biosensor, was to explore the electrode's surface functionalisation. The aim of this procedure is to insure an adequate binding of the antibody onto LIG's surface so that, later, the *E. coli* cells are immobilised onto the electrodes surface through binding between its antigens and

the aactivated antibody. Therefore, the functionalisation process was subdivided in the four steps: hydroxylation, APTES silanization, antibody immobilisation and BSA passivation.

As already mentioned in section 4.2, the hydroxylation was carried out through Fenton reaction with the intention of increasing the density of hydroxyl groups on LIG's surface. So, to analyse the performance of such reaction, Raman and X-ray photon spectroscopies were used. Besides, since in section 5.1 the value of the A_{eff} of LIG electrodes was ascribed to low wettability of the same, one also resorted to electrochemical characterisation of LIG after the Fenton reaction to clarify this question.
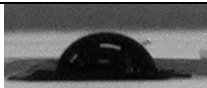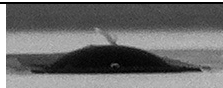
Regarding Raman characterisation, the spectra acquirement followed the procedure used in section 5.1. The obtained results were similar to the spectrum in **Figure 4.3**-(b). It was expected an increase of the D band intensity, since it is known that this reaction attacks the sp^2 carbon, bonding OH groups to it, and, consequently, turning it sp^3 hybridised [147], [148]. Accordingly, it would promote a higher ratio I_D/I_G. In **Table 4.3**, both intensity ratios of LIG prepared at 250 mm/s before and after being submitted to the Fenton reaction are presented. From these results, it is perceptive that the effect of the reaction was not as strong as expected.

Table 4.3: Intensity ratios I_D/I_G and I_{2D}/I_G of LIG prepared at 250 mm/s before and after Fenton reaction.

	Bare LIG (250 mm/s)	LIG (250 mm/s) after Fenton
I_D/I_G	0.29 ± 0.08	0.35 ± 0.04
I_{2D}/I_G	0.40 ± 0.04	0.44 ± 0.02

Likewise, the electrochemical characterisation of the LIG electrode after hydroxylation emphasised the similarity between the LIG electrode before and after the Fenton reaction. In **Table 4.4** the k^0, A_{eff} and γ_{dl} obtained for hydroxylated LIG are compared with the ones obtained in section 5.1 for bare LIG. In addition, in this table images for qualitative evaluation of the contact angle are shown, allowing one to conclude that the obtained low effective electroactive area is not related with the surface's wettability. The latter consisted on a quick and simple procedure by placing a 50 µL drop of DI water on the electrochemical area of the electrode and photographing it with a cellphone camera, roughly aligned with the electrode plane.

Table 4.4: k^0, A_{eff}, γ_{dl} and images for qualitative evaluation of the contact angle of LIG electrode prepared at 250 mm/s before and after hydroxylation (Fenton reaction).

	Bare LIG (250 mm/s)	LIG (250 mm/s) after Fenton
k^0 (cm/s)	1.42± 0.52	1.41 ± 0.31
A_{eff} (cm^2)	2.57 ± 0.07	2.66 ± 0.03
γ_{dl} (µF/cm^2)	90.32 ± 6.19	101.54 ± 9.87

Considering these analyses, it is conspicuous that the Fenton reaction did not enhance the number of hydroxyl groups on the surface of the electrode. However, to develop a more defined and certain conclusion, XPS analysis was performed.

Concerning the XPS study, it was taken into consideration some reports that lively recommend to perform the APTES functionalisation immediately after the hydroxylation step [122], to

guarantee the formation of an uniform amine-terminated self-assembled monolayer on the surface of the electrode. Actually, this is the final purpose of the hydroxylation step. So, to study the effective impact of the Fenton reaction with XPS, two APTES (1%) functionalised electrodes were analysed: one that was hydroxylated before the silanization and another not. In **Figure 4.12**, the obtained XPS spectra, and respective fitted peaks, for both APTES-modified electrodes are shown.
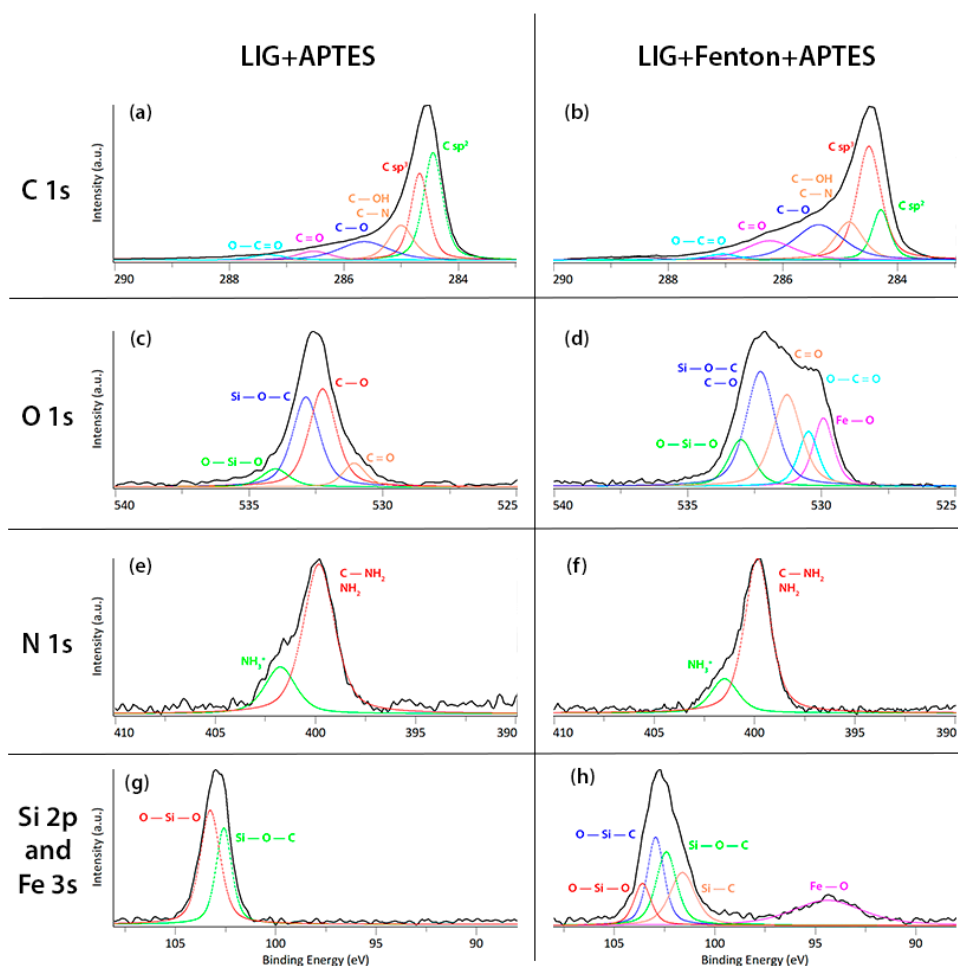
Figure 4.12: C 1s (a, b), O 1s (c, d) N 1s (e, f) and Si 2p:Fe 3s (g, h) regions of the XPS spectra (black lines) of both LIG electrodes after APTES functionalisation, the non hydroxylated (left side) and the hydroxylated (right side). The respective fitted peaks are the coloured lines.

Regarding the C 1s region (**Figure 4.12**-a, b) and comparing with the bare LIG electrode (**Figure 4.1**-a), although it is clear the increase of sp^3 hybridised carbon (red line), epoxy and ether groups (dark blue line) as well as the carbonyl groups (pink line) are more abrupt for the hydroxylated electrode. In fact, the hydroxylated electrode presents a higher sp^3 hybridised carbon peak in comparison with the sp^2 hybridised one. In the case of the O 1s region (**Figure 4.12**-c, d), the non-hydroxylated electrode (c) presented evident APTES contributions with the high intensity peak at ~532.8 eV, corresponding to Si-O-C (dark blue line), and the suppressed peak at ~534.0 eV assigned to O-Si-O groups (green line) [149]–[151]. Similarly, the peaks ascribed to C-O (red line) and C=O (light orange line) also follow the same tendency, in which the former presents a high intensity peak and the latter a much lower. In contrast, the O 1s spectrum region of the electrode submitted to Fenton reaction (**Figure 4.12**-d) exhibits a much higher contribution of the carbonyl groups (C=O, light orange line) at ~531.3 eV [152]. In addition, it also presents other two peaks, one corresponding

to carboxylic groups (light blue line), at ~530.5 eV, and another associated to the presence of iron oxide (Fe-O, pink line), at ~529.9 eV [153]. Regarding the high intensity peak at ~532.3 eV, this was assigned to both Si-O-C and C-O groups, since it was not possible to distinguish both for the fitting. To complement this information, the analysis of the Si 2p region (**Figure 4.12**-g, h) emphasizes the presence of groups such as Si-O-C, at ~102.6 eV, and O-Si-O, at ~103.3 eV, [150], [154] as in the case of non-hydroxylated electrode (**Figure 4.12**-g). In the case of the hydroxylated one (**Figure 4.12**-h), once again the proportions in terms of peak intensities diverse from the one before. Other contributions arise, both from APTES presence as in the case of Si-C, at ~101.6 eV, [154] and O-Si-C bonding, at ~ 102.9 eV, as well as from the presence of contaminants, such as Fe- O, at ~94.4 eV [155]. Lastly, the signal captured in the N 1s region confirms, for both electrodes, the presence of APTES by the emergence of two peaks at ~399.9 and ~401.6 eV addressed to amine groups (NH_2) and protonated amine groups (NH_3^+) [156], respectively.

To clarify the effect of the Fenton reaction, a quantification of the carbon groups was undertaken for the three explored samples, bare LIG and the two APTES-modified LIG samples. In **Figure 4.13**, it is presented a histogram displaying such quantification, confirming the oxidative effect of Fenton on LIG. In fact, a significant increase of ether (C-O) and carbonyl (C=O) groups is verified for the hydroxylated (Fenton) sample, maintaining the contribution of the hydroxyl groups (C-OH) very similar to the non-hydroxylated sample.
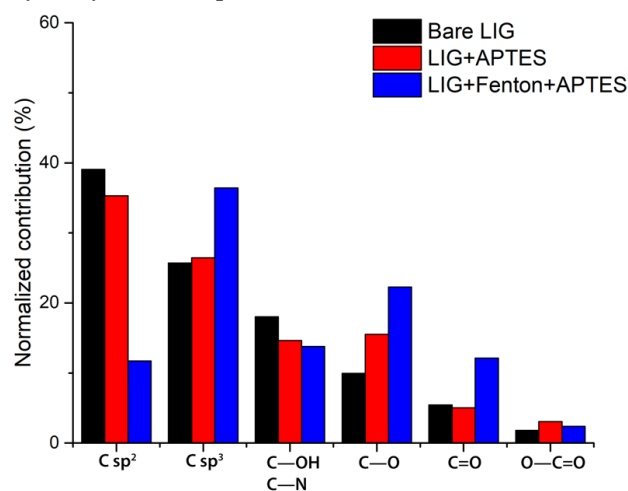
Figure 4.13: Quantitative analysis of C 1s region of the XPS spectra obtained for the bare LIG sample, in **Figure 4.11**-(a) (black) and both APTES-modified LIG, non- and hydroxylated samples, in **Figure 4.12**- (a,b) (red and blue), respectively.

In conclusion, the Fenton reaction seems that did not enhance significantly the APTES functionalisation on LIG samples, so that would not justify to include this extra step into the biosensor production. Besides, the XPS analysis confirmed that some contaminants, such as iron oxide (Fe-O), were introduced into the electrode's surface, which is not desirable. Hence, to proceed with the functionalisation, one opted to not hydroxylate the electrode.

Posteriorly, the APTES functionalisation was performed. Throughout this study, three APTES concentrations, 0.1, 1 and 10 %, were used to functionalise three LIG electrodes and to analyse the influence of such parameter, one resorted to EIS and CV electrochemical techniques. In **Figure 4.14**, the respective voltammograms and Nyquist plots are presented, comparing the three LIG electrodes before and after silanization.
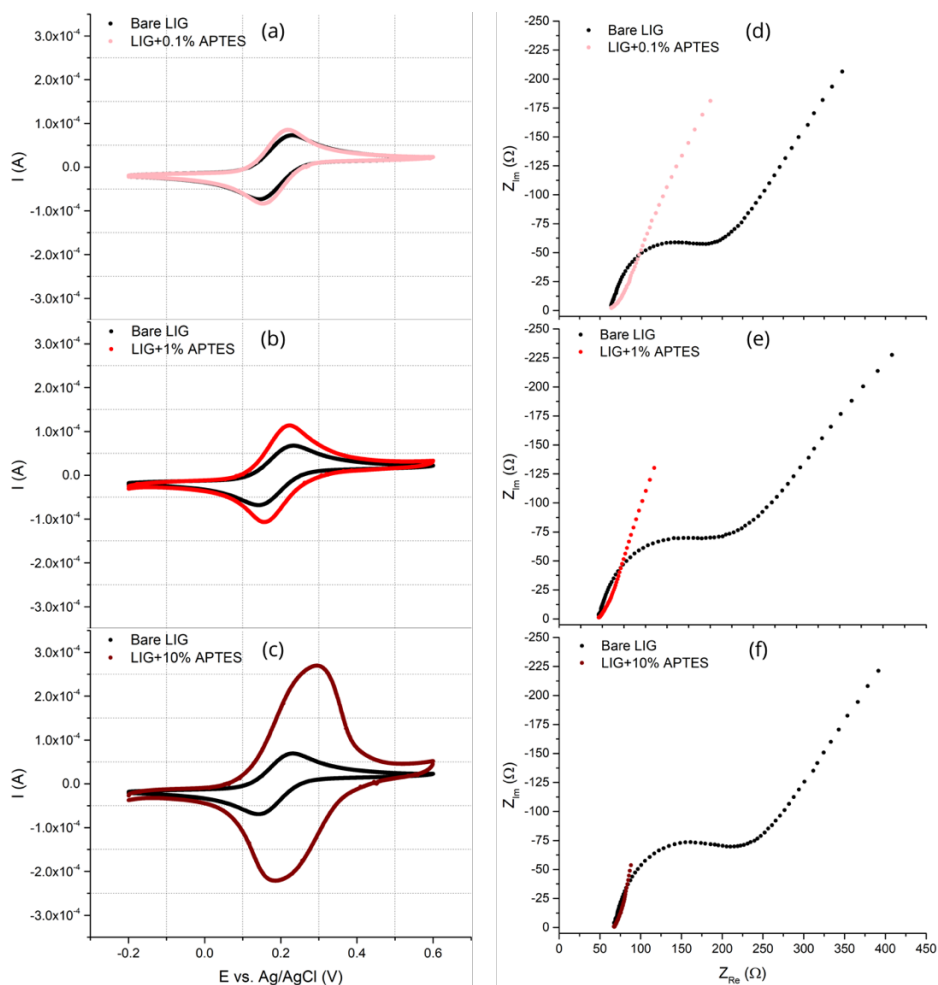
Figure 4.14: Voltammograms ((a),(b),(c)) and Nyquist plots ((d),(e),(f)) of bare LIG electrodes (black) and LIG electrodes after APTES functionalisation using 0.1% (light pink), 1% (red) and 10% (brown) concentrations. Measurements performed using $[Fe(CN)_6]^{3-/4-}$ (1:1 mM) in PBS.

Regardless the used concentration of APTES, it is evident the disappearance of the semi-circle, after the silanization (**Figure 4.14**-d, e, f). This can apparently be related to the decrease of the charge transfer resistance, R_{CT}. In fact, in terms of sensibility, it is desirable that the biosensor has a low R_{CT}. However, if this is too low, as in the case of not being able to measure it as shown in **Figure 4.14**-(d, e, f), it can complicate the analysis of the rest of the functionalisation and, afterwards, the establishment of the biosensor's limit of detection (LOD). Highlighting this behaviour, the respective voltammograms show an increase of the current response (**Figure 4.14**-a, b, c), upon APTES functionalisation. These data seem to indicate that a greater number of redox species ($[Fe(CN)_6]^{3-/4-}$) is accessing to the surface of the electrode, conflicting with the expectations of functionalisation. In fact, the concept of functionalisation relies on modifying the surface by bonding or adsorption organic and/or biomolecules to it. So, it is expected that along the functionalisation, the charge transfer between of the redox species and the electrode's surface is progressively reduced and, consequently, the R_{CT} progressively increases. Contrasting, in this case, the inverse appears to happen. Some authors have observed the same result for APTES functionalisation [157]–[161], explaining it through the polarisation of the amino groups (NH_2) in aqueous solution. As a matter of fact, this tend to protonate at pH 7.4 (NH_3^+), polarizing the surface positively, which will attract the redox species to it, by electrostatic interactions, and increase the charge transfer on the surface of

the electrode. As a result, the current response increases which can be observed within the voltammograms and the impedance spectra. Nevertheless, to confirm and clarify the electrochemical properties of the APTES-modified LIG electrodes, one obtained the k^0, A_{eff} and γ_{dl} for the 0.1 and 1% APTES-modified electrodes, since the current and impedance responses of the 10% were too accentuated, i. e. the voltammetric response was very high and the impedimetric signal presented a neglected R_{CT}. Consequently, implying loss of sensibility for further functionalisation using CV and EIS measurements.

Since for the study of APTES functionalisation, a new batch of LIG electrodes was produced, one of these new bare LIG electrodes was also submitted to the electrochemical characterisation to assure maintenance of the electrochemical properties. Therefore, in **Figure 4.15**, the obtained results for each electrochemical parameter k^0 (a), A_{eff} (b) and γ_{dl} (c) are presented, comparing the two concentrations APTES functionalised electrodes and the two bare LIG electrodes (section 5.1) electrodes and the new batch).
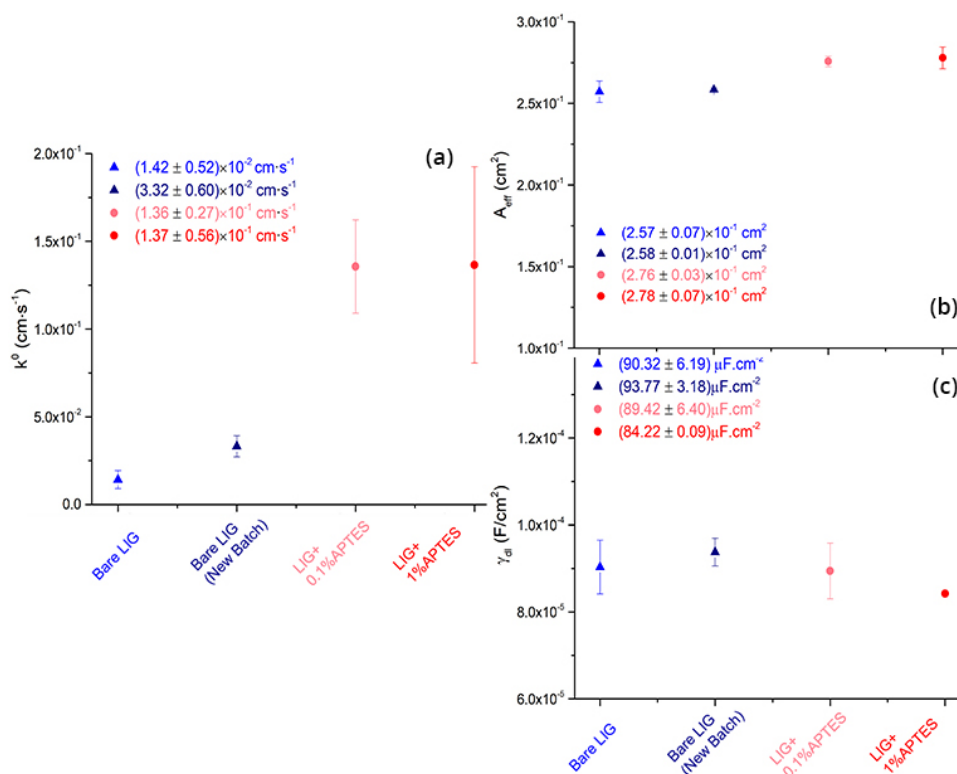
Figure 4.15: Electrochemical characterisation of the APTES-modified LIG electrodes, with 0.1 (•) and 1% (•) concentrations. For each of the parameters, k^0 (a), A_{eff} (b) and γ_{dl} (c), the obtained results for the bare LIG electrode (triplicates) in section 5.1 (▲) and for a bare LIG electrode of the new batch produced for functionalisation (▲) are shown for comparison.

Concerning the bare LIG electrodes, the results for the new batch are very similar to the one analysed in section 5.1, with exception of the heterogeneous charge transfer rate that is slightly higher for the new one. Interestingly and confirming the behaviour observed for CV and EIS measurements, both the APTES-modified electrodes display significantly higher k^0 values. Regarding the A_{eff} and γ_{dl}, the values obtained for these functionalised electrodes are very similar to the ones of the bare LIG electrodes. Hence, in terms of electrochemical parameters, one did not note considerable differences between using 0.1% or 1% APTES for its functionalisation.

Therefore, one opted to follow the 0.1% APTES functionalisation, since it guarantees for the rest of the functionalisation a measurable R_{CT} and, consequently, a measurable sensitivity, using only $\frac{1}{10}$ of the quantity of APTES.

Finally, the last two steps of functionalisation were implemented and characterised. Both anti-*E. coli* (biological recognition element) immobilisation and bovine serum albumin (BSA) passivation were performed using drop casting technique and were characterised through EIS and CV measurements, employing $[Fe(CN)_6]^{3-/4-}$ (1:1 mM) in PBS (10 mM) as electrolyte. Firstly, a 50 μL drop of anti-*E. coli* (0.5 mg/mL) solution, including NHS and EDC to assure covalent immobilisation, was deposited on the APTES-modified LIG surface. Subsequently, a 50 μL drop consisting on 1% BSA solution was casted on the resulting surface of the electrode, to block charge transfer and bacteria adsorption on the electrodes' surface, where antibody was not immobilised. Both procedures were specified in section 4.2. In **Figure 4.16**, the performed voltammetric (CV) and impedimmetric (EIS) measurements, for each functionalisation step, are shown.
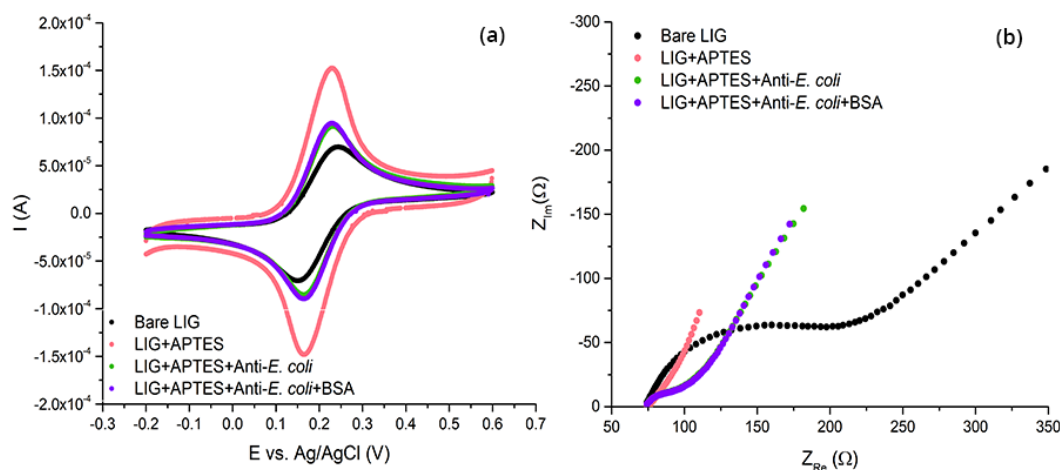
Figure 4.16: Characterisation of the functionalisation steps, comprising APTES, anti-*E. coli* and BSA, through (a) cyclic voltammetry and (b) electrochemical impedance spectroscopy, using $[Fe(CN)_6]^{3-/4-}$ (1:1 mM) in PBS (10 mM) as electrolyte.

The immobilisation of the antibody increased the R_{CT} of the electrode, as one can verify in **Figure 4.16**-(b) by the appearance of the semi-circle. This result is corroborated by the current drop on the voltammogram in **Figure 4.16**-(a). Similarly, it would be expected that after BSA passivation the R_{CT} would increase and the current would decrease. However, in **Figure 4.16**, this is not perceptive. In fact, both R_{CT} and current maintain similar values after the passivation. This result can be associated with the fact that the sites where no antibody was immobilised were not contributing significantly to the charge transfer process. Some authors have published perceptively increases of R_{CT} along with very similar current response [112], [116].

Therefore, a functionalisation protocol was defined and characterised for the development of an impedimetric immunosensor based on LIG electrodes for detection of *Escherichia coli*, consisting on three steps: APTES silanization, antibody immobilisation and BSA passivation (**Figure 3.4**).

5.3   Biosensing Response

Regarding the biosensing response of fully functionalised LIG electrodes, a set of *Escherichia coli* (ECR 1) concentrations was established (5, 10, 10^2, 10^3, 10^4, 10^5, 10^6 CFU/mL) as well as control

electrodes, verifying the selectivity and specificity of the produced biosensor towards the *E. coli* (**Table 3.1**), as stated in section 4.3. Accordingly, the set comprised two fully functionalised electrodes, one tested with ECR 1 (Biosensor) and another with *Shewanella* (Selectivity), and two controls, one without anti-*E. coli* (Control$_{\text{No Anti-}E.\ coli}$) and another where EDC and NHS were not used during anti-*E. coli* immobilisation (Control$_{\text{No EDC/NHS}}$). For each of the mentioned electrodes, EIS measurements were performed before being in contact with any *E. coli* solution (referred as blanks) and after being submitted to each of the *E. coli* concentrations, using $[\text{Fe(CN)}_6]^{3-/4-}$ (1:1 mM) in PBS (10 mM) as electrolyte. In **Figure 4.17**-(a), the Nyquist plots obtained for the tests performed with the Biosensor are shown, as an example. Unexpectedly, it is noticeable that upon *E. coli* immobilisation, the semi-circle region of the Nyquist plot diminishes, corresponding to a decrease in the charge transfer resistance, R_{CT}. Nonetheless, one proceeded with fitting the obtained results, allowing an evaluation of the normalised biosensing response, considering the biosensors and controls tested. In fact, the biosensing response, as exposed in section 2.2, is assumed by the R_{CT} value extracted from the Nyquist plots by fitting it to an equivalent circuit, which for faradaic impedance-based sensors is commonly the modified-Randles circuit (**Figure 2.2**). However, during functionalisation and *E. coli* testing, the obtained Nyquist plots showed a phase deviation of the part related to the diffusion controlled region (**Figure 4.17**-a), which is normally described by a Warburg element. The latter is defined by a constant $\frac{\pi}{4}$ phase. Therefore, to accomplish a more suitable fitting, a new equivalent circuit was considered, in which the Warburg element was substituted by a constant phase element (CPE), and is presented as an inset in **Figure 4.17**-(b), along with the Nyquist plot of the Biosensor blank test and respective fitting, as an example.

All the fittings were executed using EIS Spectrum Analyser 1.0 program and all the fitted spectra had a relative deviation from the obtained experimentally lower than 2%.
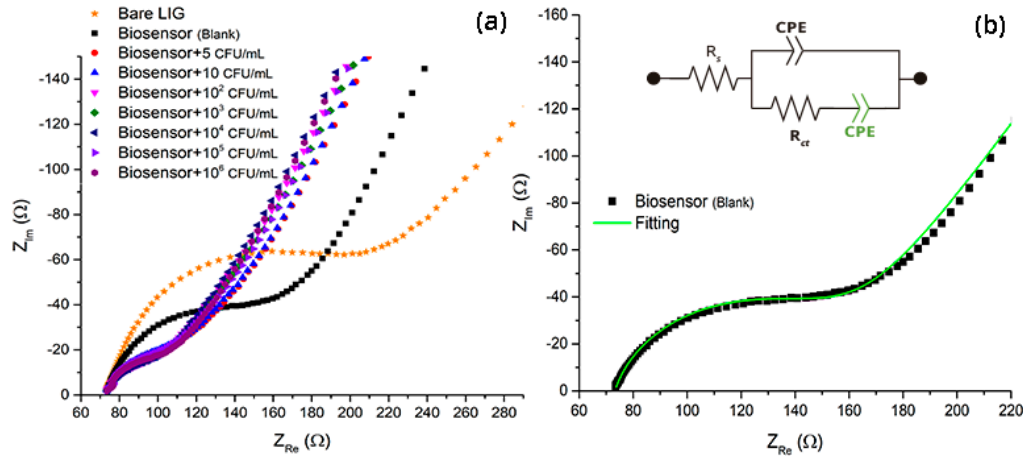
Figure 4.17: (a) Obtained Nyquist plots for the EIS measurements performed with the Biosensor before (blank) and after being in contact with *E. coli* concentrations, using $[\text{Fe(CN)}_6]^{3-/4-}$ (1:1 mM) in PBS (10 mM) as electrolyte. (b) Nyquist plot obtained for the Biosensor's blank test and respective fitted spectrum, accomplished considering the equivalent circuit.

Subsequently, the normalised biosensing response (R_{CT}) was established through (eq. 4.6) and it is presented in **Figure 4.18** for the tested biosensors (Biosensor and Selectivity) and controls (Control$_{\text{No EDC/NHS}}$ and Control$_{\text{No Anti-}E.\ coli}$).

$$\frac{\Delta R_{CT}}{R_{CT}^{blank}} = \frac{|R_{CT} - R_{CT}^{blank}|}{R_{CT}^{blank}} \qquad \text{(eq. 4.6)}$$
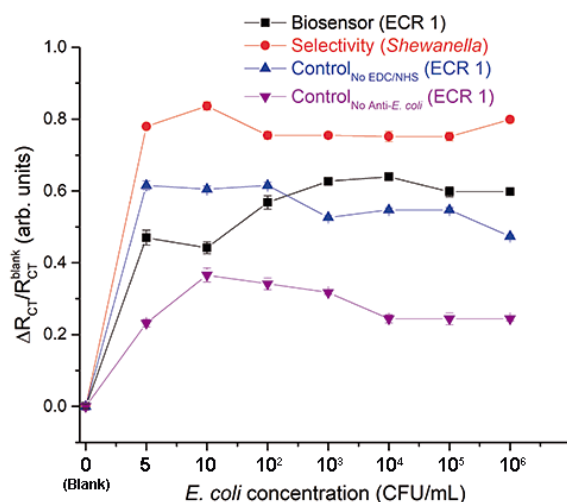
Figure 4.18: Normalised biosensing response, R_{CT} variation, of the fully functionalised biosensors (Biosensor and Selectivity) and controls (Control$_{No\ EDC/NHS}$ and Control$_{No\ Anti\text{-}E.\ coli}$) before (blank) and upon contact with 5, 10, 10^2, 10^3, 10^4, 10^5 and 10^6 CFU/mL of *E. coli* in 10 mM PBS solution.

Unfortunately, the normalised Biosensor response does not clarify the odd behaviour already spotted in **Figure 4.17**-(a). As a matter of fact, in **Figure 4.18**, the Biosensor response is undistinguishable from the Selectivity and Controls one, not being clear a specific R_{CT} variation. Consequently, it is not conclusive if the produced biosensors can detect *E. coli*. Therefore, in order to assuredly acknowledge if the produced biosensors are able to detect *E. coli* and, subsequently, to explore the origin of the R_{CT} reduction upon contact with *E. coli* solution, a new set of tests was performed, which are described and discussed in the next section (5.4).
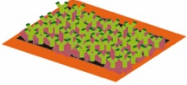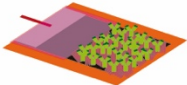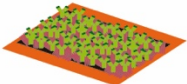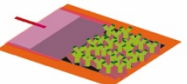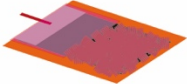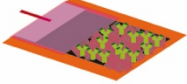
5.4 Evidence of *E. coli* detection

The bizarre behaviour of the biosensing response, led us to perform a confirmatory analysis to guarantee the detection of *E. coli*, using the produced LIG impedimetric immunosensors. First, a brief analysis concerning the origin of such behaviour was done. Since nothing in the functionalisation protocol seemed to be erratic, particularly taking into consideration the characterisation explored throughout section 5.2, a new plan to evaluate the effectiveness of the antibody-antigen interaction was delineated taking into account the sufficiency of the quantity of antibody available to bound and the ability of the medium (PBS) to interact with the biosensor.

The new batch of biosensors was produced with the intent of being tested towards 10^6 CFU/mL of *E. coli* solution (in 10 mM PBS), using two different strains, ECR 1 and a second *E. coli* strain ECR 15 since both have the same type of antigens, K and O. The proof of *E. coli* detection was settle on a series of tests: electrochemical impedance spectroscopy (EIS) measurements, bacterial DNA test and scanning electron microscopy (SEM) visualisation. The new set of biosensors was functionalised accordingly with the protocol discussed before (section 4.2), except for the samples prepared for DNA testing and the two biosensors produced for analysing the sufficiency of antibody quantity, for which the concentration of anti-*E. coli* used was doubled (~1 mg/mL), as designated in **Table 4.5**. The procedure to obtain the 10^6 CFU/mL concentration of both *E. coli,* ECR 1 and ECR 15, was the same as described in section 4.3. Similarly, the bacteria immobilisation onto the biosensors and samples prepared for DNA testing also followed the same protocol described previously (section 4.3), for which each sample and biosensor was dipped in the respective

10^6 CFU/mL solution for 45 minutes. Then, they were rinsed with PBS and dried with a gentle N_2 flow. Afterwards, for preservation purposes, the samples for DNA testing were conserved in PBS at ~4 ˚C.

Table 4.5: New set of biosensors produced and respective tests performed as well as the designated target bacteria used.

	DNA Tests	EIS and SEM Tests	Target Bacteria
Biosensor (~1 mg/mL anti-*E. coli*)			*E. coli* (ECR 1)
Biosensor (~1 mg/mL anti-*E. coli*)			*E. coli* (ECR 15)
Control (No anti-*E. coli*)	—		*E. coli* (ECR 1)
Biosensor (0.5 mg/mL)	—		PBS

Anti-*E.coli* ; BSA

Concerning the EIS measurements, the obtained results are presented in **Figure 4.19**. These confirm the behaviour already attained in section 5.3, proving that R_{CT} decreases after being in contact with *E. coli* solution. Further, it also confirms that the acquired response does not depend on the quantity of anti-*E. coli* immobilised on the electrodes' surface. Moreover, the biosensor tested for PBS also proved that the response is not provided from interaction between PBS and biosensor. The obtained results concerning the electrochemical test of the biosensor tested against ECR 15 are not presented, since no EIS measurement was taken for the blank biosensor, meaning before ECR 15 immobilisation.
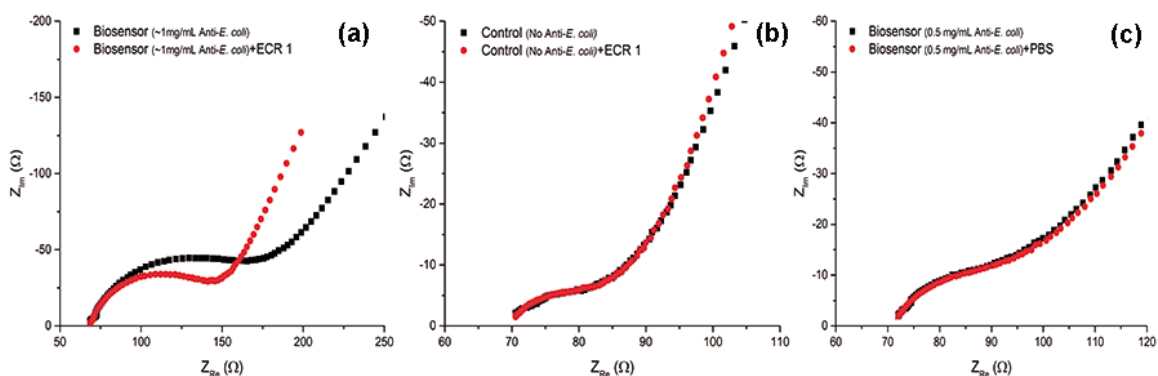
Figure 4.19: Acquired Nyquist plots for the new set of electrochemical tests before (black squares) and after (red dots) *E. coli* immobilisation, in which (a) corresponds to the biosensor functionalised with double the anti-E. coli concentration (~1 mg/mL), (b) to the control with no anti-*E. coli* functionalised and (c) to the biosensor with the regular functionalisation protocol (0.5 mg/mL of anti-*E. coli*). The measurements were performed using $[Fe(CN)_6]^{3-/4-}$ (1:1 mM) in PBS (10 mM) as electrolyte.

Regarding the DNA tests, the purpose of such tests was to verify the presence of *E. coli* after its immobilisation onto the biosensor, confirming that the response obtained through EIS

measurements can be directly related to the *E. coli* detection. Further, two different strains of *E. coli* were tested, ECR 1 and ECR 15, with the aim of proving the effectiveness of the antibody-antigen interaction, since both strains present antigens K and O specific for the immobilised anti-*E. coli* (polyclonal anti-*E. coli* K/O). The DNA tests were performed by the Microbiology group from University Aveiro (http://biomicerolab.web.ua.pt/). These tests can be divided in three major parts DNA extraction, DNA amplification and DNA separation and staining. Initially, the DNA extraction was performed using MoBio Power Soil DNA Purification Kit, acquired from MoBio. Afterwards, the extracted and purified DNA segments were amplified through polymerase chain-reaction (PCR), targeting two envisioned genes for each sample: a general one that codifies for ribosomal RNA subunit 16S, present in all bacteria; and a specific one that codifies for a beta-lactamase of CTX-M type (bla_{CTX-M}), corresponding to more specific antibiotic resistance genes previously detected in both strains ([124], $bla_{CTX-M-15}$ in ECR 1 and $bla_{CTX-M-32}$ in ECR 15). Lastly, the resultant DNA segments were separated by electrophoresis in agarose gel (1.5%) scanned with 90 V for 1h and stained with ethidium bromide. Then, by UV fluorescence, (Gel Doc system, Bio-Rad) the amplified DNA segments can be distinguish, as in **Figure 4.20**.
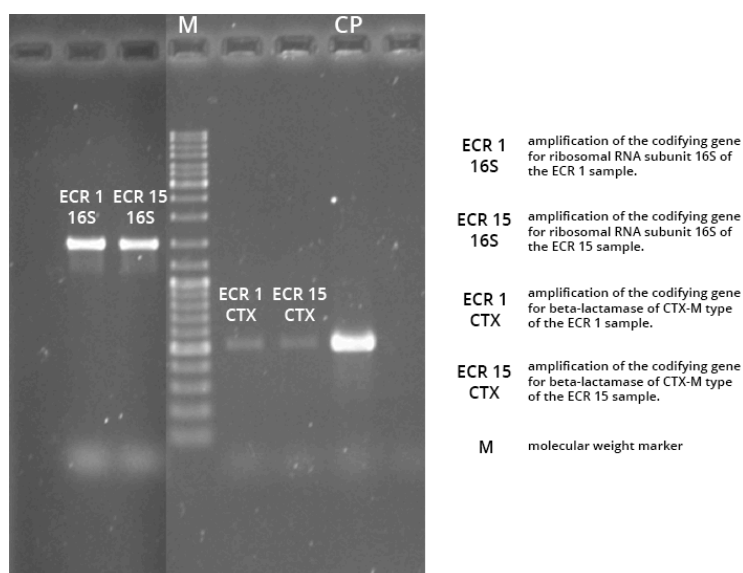
Figure 4.20: Result of the PCR amplification of DNA extracted from biosensor samples immobilised with ECR 1 and ECR 15, separated in an agarose gel (1.5%) at 90 V for 1 h.

In **Figure 4.20**, it is confirmed the strong presence of bacteria in both samples, by the high intensities of the amplification of the codifying gene for ribosomal RNA subunit 16S (ECR 1-16S and ECR 15-16S). More specifically, the amplification of the codifying gene for CTX-M beta-lactamase strongly suggests that the bacteria present in the samples correspond to ECR 1 and ECR 15, respectively. Thus, one can conclude that the functionalisation protocol used and characterised throughout this thesis is suitable to immobilise *E. coli*.

Finally, after the EIS measurements each biosensor was submitted to fixation and dehydration protocol with the goal of visualizing *E. coli* cells on the biosensors' surface through SEM analysis. So, the biosensors were dipped in a glutaraldehyde (2.5%) solution overnight, at ~4 °C, in order to inhibit the bacteria from lysing and to preserve its morphology throughout dehydration and SEM analysis. Then, each of the latter was submitted to a dehydration procedure, assuring that the bacteria would not blast when in vacuum environment. This consisted in dipping each biosensor in ethanol solutions with different concentrations, 50, 70, 80, 90 and 100%, in ascending order, for 30, 15, 15,

15 and 15 minutes, respectively, repeating the last concentration. Further, the biosensors were dried with a gentle N_2 flow and kept at ~4 °C. Regarding the SEM analysis, several factors were required to be taken into consideration. To start, the biosensors' electroactive area is 5 x 5 mm^2 and an *E. coli* cell has, approximately, 1 x 2 μm^2, constituting a tremendous effort to scan meticulously the entire area to find *E. coli* cells. Further, the LIG's surface has very porously morphology along with finely disorder structure (**Figure 4.21**-a), complicating to differentiate the cells from the unique surface structure. However, great endeavour was put on such analysis and, fortunately, a SEM image of a single *E. coli* cell was taken from the biosensor targeting ECR 1 and is presented in **Figure 4.21**-(b).
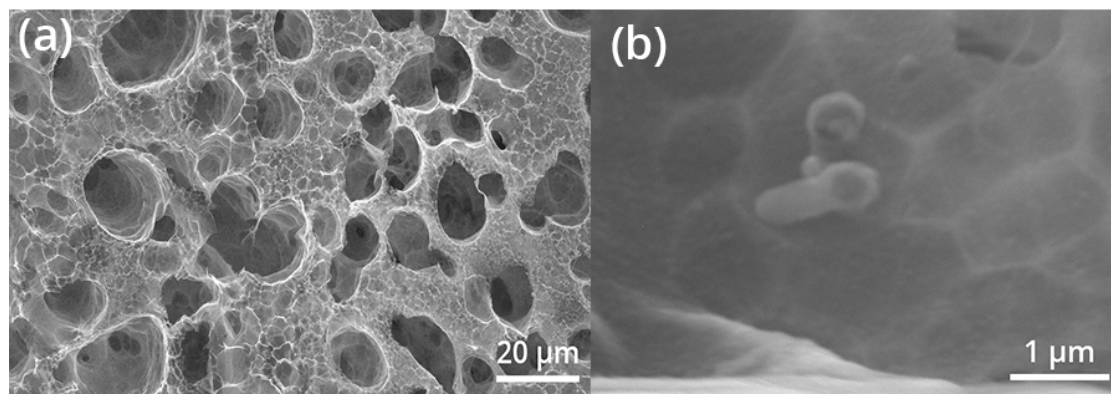
Figure 4.21: SEM images of (a) the porously morphology and finely structure of the biosensors' surface and (b) a perceptively curved *E. coli* cell on the biosensor's surface.

In conclusion, these confirmatory tests enabled to evidence that the produced LIG impedimetric immunosensors detect *E. coli*. However, regarding the impedimetric biosensing response, further tests need to be done in order to obtain a distinguishable response in terms of selectivity and false-positives (controls), confronting the obtained results in **Figure 4.18**. Even though, these tests also verified that the corresponding response manifests through decreasing of the charge transfer resistance, R_{CT}. The latter constitutes an unexpected result, since it was envisioned and verified by other impedimetric biosensors for *E. coli* detection that these bacteria, once immobilised onto the electrode's surface, consist on a charge transfer barrier, thus increasing the R_{CT} value. However, EIS measurements were performed using an AC input signal of 5 mV amplitude, alternating around a DC bias that assumed the electrochemical cell's OCP value, ~190 mV. Until now, this DC bias has been neglected, but since *E. coli* cells are attached to the biosensor's surface through antibody-antigen interaction, this might become a point to be noted. In fact, most of the DC potential drop is experienced at the working electrode's interface [63], so, it is quite probable that the bacteria are perceiving it. In that case, it has been thought that the DC bias might be inducing a transmembrane potential on *E. coli*'s membrane. In fact, it has been reported that *E. coli* cells with incubation times, for culture enrichment, similar to the ones used in this work (~16h) have a membrane potential between -140 and -160 mV, approximately [162]. Thus, upon EIS measurements the cells were subjected to a ~190 mV DC bias, which would change the membrane potential and, consequentially, enable the transport of some cations, mainly potassium (K^+) and sodium (Na^+) [162], [163], to the nearby external environment of the bacteria, which is the biosensor's surface. Consequentially, along with this hypothesis, it is considered that these liberated substances would exercise an electrostatic attraction on the redox probe ($[Fe(CN)_6]^{3-/4-}$), as verified for APTES, enhancing the charge transfer and diminishing the R_{CT}.

VI | Conclusions and Future Work

The main goal of this work was to develop a LIG-based impedimetric immunosensor for *Escherichia coli* detection.

At first, LIG electrodes were produced, fixating all the laser parameters with exception of the laser scan speed, v_{laser}, for which five values (150, 200, 250, 300 and 350 mm/s) were explored. The comprehensive characterisation enabled to establish that in fact these laser parameters allow to produce laser-induced graphene electrodes with high heterogeneous charge transfer rate constant, k^0, which is determinant for well-succeeded impedimetric sensors. Particularly, one concluded that the 250 mm/s v_{laser} generated the most suitable electrodes to proceed with functionalisation.

Secondly, a four steps functionalisation protocol was thoroughly analysed with the purpose of having an efficient LIG immunosensor for *E. coli*. Regarding the adequacy of LIG's hydroxylation, one confirmed that this was not a mandatory step, having LIG sufficient hydroxyl groups to follow functionalisation. Then, the following steps, APTES (0.1%) silanization, anti-*E. coli* (0.5 mg/mL) immobilisation and BSA (1%) passivation were successfully achieved and characterised, qualifying the functionalised electrodes to be tested with respect to its biosensing response.

Finally, the prepared biosensors were submitted to different *E. coli* solution concentrations and tested through EIS, resulting in an ambiguous biosensing response, inconclusive towards *E. coli* detection. Therefore, extra tests were performed, exploring the ability of the produced sensors to detect *E. coli*. The obtained results clearly confirmed that the prepared biosensors were able to detect the target bacteria. However, further studies testing selectivity and false-positive responses are required in order to securely prove these electrodes as *E.coli* biosensors. Besides, considering the work developed and discussed during this thesis, further experiments and tests should be examined towards the optimisation of these biosensors. The following suggestions should be considered as future work:

- Reduce the electrodes' electrochemical area in order to increase the R_{CT} and have a better control of the whole functionalisation, especially after APTES silanization;

- Study different protocols of the Fenton reaction and other hydroxylation procedures, to assure the upper limit of hydroxyl groups on LIG's surface for further functionalisation steps;

- Investigate the ability of the biosensor to distinguish different concentrations of *E. coli* and optimise it;

- Understand and explore the integration of such biosensors in water quality monitoring systems.

VII | References

[1] "United Nations Secretary-General's Plan: Water Action Decade 2018-2028," 2018.

[2] *Safely managed drinking water - thematic report on drinking water 2017.* Geneva, Switzerland: World Health Organization, 2017.

[3] *Assessing Microbial Safety of Drinking Water - Improving Approaches and Methods.* Published on behalf of World Health Organization and the Organisation for Economic Co-operation and Devalopment by IWA Publishing, 2003.

[4] *Guidelines for drinking-water quality.*, 4th ed. Geneva, Switzerland: World Health Organization, 2011.

[5] A. Ahmed, J. V. Rushworth, N. A. Hirst, and P. A. Millner, "Biosensors for whole-cell bacterial detection," *Clin. Microbiol. Rev.*, vol. 27, no. 3, pp. 631–646, 2014.

[6] A. Rompré, P. Servais, J. Baudart, M. R. De-Roubin, and P. Laurent, "Detection and enumeration of coliforms in drinking water: Current methods and emerging approaches," *J. Microbiol. Methods*, vol. 49, no. 1, pp. 31–54, 2002.

[7] A. K. Deisingh and M. Thompson, "Biosensors for the detection of bacteria.," *Can. J. Microbiol.*, vol. 50, no. 2, pp. 69–77, 2004.

[8] S. Brosel-Oliu, N. Uria, N. Abramova, and A. Bratov, "Impedimetric Sensors for Bacteria Detection," in *Biosensors - Micro and Nanoscale Applications*, T. Rinken, Ed. InTechOpen, 2015.

[9] R. E. Ionescu, "Biosensor platforms for rapid detection of E. coli Bacteria," in *Salmonella: A Dangerous Foodborne Pathogen*, 2012.

[10] F. Cheng Y, "Biosensors for Bacterial Detection," *Int. J. Biosens. Bioelectron.*, vol. 2, no. 6, pp. 7–9, 2017.

[11] J. W. Lim, D. Ha, J. Lee, S. K. Lee, and T. Kim, "Review of Micro/Nanotechnologies for Microbial Biosensors," *Front. Bioeng. Biotechnol.*, vol. 3, no. May, pp. 1–13, 2015.

[12] N. Sanvicens, C. Pastells, N. Pascual, and M. P. Marco, "Nanoparticle-based biosensors for detection of pathogenic bacteria," *TrAC - Trends Anal. Chem.*, vol. 28, no. 11, pp. 1243–1252, 2009.

[13] R. Săndulescu, M. Tertiş, C. Cristea, and E. Bodoki, "New Materials for the Construction of Electrochemical Biosensors," in *Biosensors - Micro and Nanoscale Applications*, T. Rinken, Ed. InTechOpen, 2015, pp. 1–36.

[14] C. Cristea and V. Ha, "Electrochemical Sensor and Biosensors," in *Environmental Analysis by Electrochemical Sensors and Biosensors*, L. M. Moretto and K. Kalcher, Eds. Springer, 2014, pp. 155–165.

[15] S. F. D. Souza, "Microbial biosensors," *Biosens. Bioelectron.*, vol. 16, pp. 337–353, 2001.

[16] S. Vigneshvar, C. C. Sudhakumari, B. Senthilkumaran, and H. Prakash, "Recent Advances in Biosensor Technology for Potential Applications - An Overview.," *Front. Bioeng. Biotechnol.*, vol. 4, no. February, p. 11, 2016.

[17] C. Cristea, B. Feier, and R. Sandulescu, "Electrochemical Sensors in Environmental Analysis," in *Environmental Analysis by Electrochemical Sensors and Biosensors*, L. M. Moretto and K. Kalcher, Eds. Springer, 2014, pp. 167–191.

[18] H. Yang, H. Zhou, H. Hao, Q. Gong, and K. Nie, "Detection of Escherichia coli with a label-free impedimetric biosensor based on lectin functionalized mixed self-assembled monolayer," *Sensors Actuators, B Chem.*, vol. 229, pp. 297–304, 2016.

[19] B. A. G. Rodriguez, E. K. G. Trindade, D. G. A. Cabral, E. C. L. Soares, C. E. L. Menezes, D. C. M. Ferreira, R. K. Mendes, and R. F. Dutra, "Nanomaterials for Advancing the Health Immunosensor," in *Biosensors - Micro and Nanoscale Applications*, T. Rinken, Ed. InTechOpen, 2015.

[20] N. F. Atta, A. Galal, and E. H. El-ads, "Graphene — A Platform for Sensor and Biosensor Applications," in *Biosensors - Micro and Nanoscale Applications*, T. Rinken, Ed. InTechOpen, 2015.

[21] C. I. L. Justino, A. R. Gomes, A. C. Freitas, A. C. Duarte, and T. A. P. Rocha-Santos, "Graphene based sensors and biosensors," *TrAC Trends Anal. Chem.*, vol. 91, pp. 53–66, Jun. 2017.

[22] C. S. Park, H. Yoon, and O. S. Kwon, "Graphene-based nanoelectronic biosensors," *J. Ind. Eng. Chem.*, vol. 38, pp. 13–22, 2016.

[23] M. Pumera, "Graphene in biosensing," *Mater. Today*, vol. 14, no. 7–8, pp. 308–315, 2011.

[24] T. J. Davies, M. E. Hyde, and R. G. Compton, "Nanotrench Arrays Reveal Insight into Graphite Electrochemistry," *Angew. Chemie Int. Ed.*, vol. 44, no. 32, pp. 5121–5126, Aug. 2005.

[25] S. C. S. Lai, A. N. Patel, K. McKelvey, and P. R. Unwin, "Definitive Evidence for Fast Electron Transfer

at Basal Plane Graphite from High Resolution Electrochemical Imaging," *Angew. Chem. Int. Ed.*, vol. 51, no. 22, pp. 5405–5408, 2012.

[26] J. Lin, Z. Peng, Y. Liu, F. Ruiz-Zepeda, R. Ye, E. L. G. Samuel, M. J. Yacaman, B. I. Yakobson, and J. M. Tour, "Laser-induced porous graphene films from commercial polymers," *Nat. Commun.*, vol. 5, Dec. 2014.

[27] S. Octavia and R. Lan, "The family Enterobacteriaceae," in *The Prokaryotes: Gammaproteobacteria*, 4th ed., E. Rosenberg, E. F. DeLong, S. Lory, E. Stackebrandt, and F. Thompson, Eds. Springer, 2014, pp. 225–286.

[28] C. Baylis, M. Uyttendaele, H. Joosten, A. Davies, and H. J. Heinz, *The Enterobacteriaceae and their significance to the food industry*. 2011.

[29] "Microbial fact sheets," in *World Health Organization Guidelines for Drinking*, 4th ed., World Health Organization, 2011, pp. 231–306.

[30] J. Min and A. J. Baeumner, "Highly sensitive and specific detection of viable Escherichia coli in drinking water.," *Anal. Biochem.*, vol. 303, no. 2, pp. 186–93, 2002.

[31] C. Gleeson and N. Gray, *The Coliform Index and Waterborne Disease: Problems of microbial drinking water assessment (Google eBook)*. 2002.

[32] "Microbial Aspects," in *World Health Organization Guidelines for Drinking*, 4th ed., World Health Organization, 2011, pp. 117–153.

[33] M. T. Madigan, J. M. Martinko, K. S. Bender, D. H. Buckley, and D. A. Stahl, *Brock Biology of Microorganisms*. Pearson Education, Inc., 2015.

[34] ISO 6222:1999, *Water quality — Enumeration of culturable micro-organisms — Colony count by inoculation in a nutrient agar culture medium.* .

[35] ISO 9308-2:2012, *Water quality — Enumeration of Escherichia coli and coliform bacteria — Part 2: Most probable number method.* .

[36] D. Burdass, J. Grainger, and J. Hurst, Eds., *Basic Practical Microbiology - A Manual*. Society for General Microbiology (SGM), 2006.

[37] ISO 9308-1:2014, *Water quality — Enumeration of Escherichia coli and coliform bacteria — Part 1: Membrane filtration method for waters with low bacterial background flora.* .

[38] ISO 9308-3:1998/Cor.1:2000, *Water quality — Detection and enumeration of Escherichia coli and coliform bacteria — Part 3: Miniaturized method (Most Probable Number) for the detection and enumeration of E. coli in surface and waste water.* .

[39] D. Wild, *The Immunoassay Handbook: Theory and applications of ligand binding, ELISA and related techniques*. 2013.

[40] D. Mendes Silva and L. Domingues, "On the track for an efficient detection of Escherichia coli in water: A review on PCR-based methods," *Ecotoxicol. Environ. Saf.*, vol. 113, pp. 400–411, 2015.

[41] J. G. Pacheco, M. F. Barroso, H. P. A. Nouws, S. Morais, and C. Delerue-Matos, "Biosensors," *Curr. Dev. Biotechnol. Bioeng. Bioprocesses, Bioreact. Control.*, pp. 627–648, 2016.

[42] N. J. Ronkainen, H. B. Halsall, and W. R. Heineman, "Electrochemical biosensors," *Chem. Soc. Rev.*, vol. 39, no. 5, pp. 1747–1763, 2010.

[43] B. D. Leca-Bouvier and L. J. Blum, "Enzyme for Biosensing Applications," in *Recognition Receptors in Biosensors*, M. Zourob, Ed. Springer, 2010, pp. 177–220.

[44] L. C. Clark and C. Lyons, "Electrode systems for continuous monitoring in cardiovascular surgery," *Ann. N. Y. Acad. Sci.*, vol. 102, no. 1, pp. 29–45, 1962.

[45] K. R. Rogers, "Principles of Affinity-Based Biosensors," *Mol. Biotechnol.*, vol. 14, no. 2, pp. 109–130, 2000.

[46] C. Wingren and C. Borrebaeck, "Protein microarray technologies for detection and identification of bacterial and protein analytes," in *Principles of Bacterial Detection: Biosensors, Recognition Receptors and Microsystems*, 1st ed., M. Zourob, S. Elwary, and A. Turner, Eds. Springer Science+Business Media, LLC, 2008, pp. 715–729.

[47] P. Damborsky, J. vitel, and J. Katrlik, "Optical biosensors," *Essays Biochem.*, vol. 60, no. 1, pp. 91–100, 2016.

[48] A. M. Hutchinson, "Evanescent wave biosensors," *Mol. Biotech.*, vol. 3, p. 47, 1995.

[49] J. L. Arlett, E. B. Myers, and M. L. Roukes, "Comparative advantages of mechanical biosensors," *Nat. Nanotechnol.*, vol. 6, no. 4, pp. 203–215, 2011.

[50] K. Mosbach, "Thermal biosensors," *Biosens. Bioelectron.*, vol. 6, no. 3, pp. 179–182, 1991.

[51] K. Ramanathan and B. Danielsson, "Principles and applications of thermal biosensors," *Biosens. Bioelectron.*, vol. 16, no. 6, pp. 417–423, 2001.

[52] J. B. Haun, T. J. Yoon, H. Lee, and R. Weissleder, "Magnetic nanoparticle biosensors," *Wiley Interdiscip. Rev. Nanomedicine Nanobiotechnology*, vol. 2, no. 3, pp. 291–304, 2010.

[53] D. R. Thévenot, K. Toth, R. A. Durst, and G. S. Wilson, "Electrochemical biosensors: Recommended definitions and classification," 2001.

[54] M. Maas, W. Perold, and L. Dicks, "Biosensors for the detection of Escherichia coli," *Water SA*, vol. 43, no. 4, pp. 1816–7950, 2017.

[55] A. C. Olivieri, N. M. Faber, J. Ferré, R. Boqué, J. H. Kalivas, and H. Mark, "Uncertainty estimation and figures of merit for multivariate calibration (IUPAC Technical Report)," *Pure Appl. Chem.*, vol. 78, no. 3, pp. 633–661, 2006.

[56] K. Danzer and L. A. Currie, "Guidelines for calibration in analytical chemistry. Part I. Fundamentals and single component calibration (IUPAC Recommendations 1998)," *Pure Appl. Chem.*, vol. 70, no. 4, pp. 993–1014, 1998.

[57] V. Templier, A. Roux, Y. Roupioz, and T. Livache, "Ligands for label-free detection of whole bacteria on biosensors: A review," *TrAC - Trends Anal. Chem.*, vol. 79, pp. 71–79, 2016.

[58] D. Grieshaber, R. Mackenzie, J. Vörös, and E. Reimhult, "Electrochemical Biosensors -Sensor Principles and Architectures," *Sensors*, vol. 8, no. January, pp. 1400–1458, 2008.

[59] R. Koncki, "Recent developments in potentiometric biosensors for biomedical analysis," *Anal. Chim. Acta*, vol. 599, no. 1, pp. 7–15, 2007.

[60] M. Kaisti, "Detection principles of biological and chemical FET sensors," *Biosens. Bioelectron.*, vol. 98, no. June, pp. 437–448, 2017.

[61] J. L. Hammond, N. Formisano, P. Estrela, S. Carrara, and J. Tkac, "Electrochemical biosensors and nanobiosensors," *Essays Biochem.*, vol. 60, no. 1, pp. 69–80, 2016.

[62] M. Zourob, Ed., *Recognition Receptors in Biosensors*. New York, NY: Springer New York, 2010.

[63] A. J. Bard and L. R. Faulkner, *Electrochemical methods: Fundamentals and Applications*, 2nd ed. John Wiley & Sons, Inc, 2001.

[64] H. A. Abdulbari and E. A. M. Basheer, "Electrochemical Biosensors: Electrode Development, Materials, Design, and Fabrication," *ChemBioEng Rev.*, vol. 4, no. 2, pp. 92–105, 2017.

[65] G. Maduraiveeran and W. Jin, "Nanomaterials based electrochemical sensor and biosensor platforms for environmental applications," *Trends Environ. Anal. Chem.*, vol. 13, pp. 10–23, 2017.

[66] J. Chen, S. M. Andler, J. M. Goddard, S. R. Nugen, and V. M. Rotello, "Integrating recognition elements with nanomaterials for bacteria sensing," *Chem. Soc. Rev.*, vol. 46, no. 5, pp. 1272–1283, 2017.

[67] X. Luo, A. Morrin, A. J. Killard, and M. R. Smyth, "Application of nanoparticles in electrochemical sensors and biosensors," *Electroanalysis*, vol. 18, no. 4, pp. 319–326, 2006.

[68] P. Ramnani, N. M. Saucedo, and A. Mulchandani, "Carbon nanomaterial-based electrochemical biosensors for label-free sensing of environmental pollutants," *Chemosphere*, vol. 143, pp. 85–98, 2016.

[69] S. Gupta, C. N. Murthy, and C. R. Prabha, "Recent advances in carbon nanotube based electrochemical biosensors," *Int. J. Biol. Macromol.*, vol. 108, pp. 687–703, 2018.

[70] J. Wang, "Carbon-nanotube based electrochemical biosensors: A review," *Electroanalysis*, vol. 17, no. 1, pp. 7–14, 2005.

[71] W. Zhang, S. Zhu, R. Luque, S. Han, L. Hu, and G. Xu, "Recent development of carbon electrode materials and their bioanalytical and environmental applications," *Chem. Soc. Rev.*, vol. 45, no. 3, pp. 715–752, 2016.

[72] V. Choudhary, B. P. Singh, and R. B. Mathur, "Carbon Nanotubes and Their Composites," in *Syntheses and Applications of Carbon Nanotubes and Their Composites*, no. May 2014, InTech, 2013.

[73] X. Huang, Z. Yin, S. Wu, X. Qi, Q. He, Q. Zhang, Q. Yan, F. Boey, and H. Zhang, "Graphene-based materials: Synthesis, characterization, properties, and applications," *Small*, vol. 7, no. 14, pp. 1876–1902, 2011.

[74] E. P. Randviir, D. A. C. Brownson, and C. E. Banks, "A decade of graphene research: Production, applications and outlook," *Mater. Today*, vol. 17, no. 9, pp. 426–432, 2014.

[75] V. Singh, D. Joung, L. Zhai, S. Das, S. I. Khondaker, and S. Seal, "Graphene based materials: Past, present and future," *Prog. Mater. Sci.*, vol. 56, no. 8, pp. 1178–1271, 2011.

[76] K. S. Novoselov, A. K. Geim, S. V. Morozov, D. Jiang, Y. Zhang, S. V. Dubonos, I. V. Grigorieva, and A. A. Firsov, "Electric Field Effect in Atomically Thin Carbon Films," Mar. 2004.

[77] S. Bae, H. Kim, Y. Lee, X. Xu, J. S. Park, Y. Zheng, J. Balakrishnan, T. Lei, H. Ri Kim, Y. Il Song, Y.

J. Kim, K. S. Kim, B. Özyilmaz, J. H. Ahn, B. H. Hong, and S. Iijima, "Roll-to-roll production of 30-inch graphene films for transparent electrodes," *Nat. Nanotechnol.*, vol. 5, no. 8, pp. 574–578, 2010.

[78] V. Y. Aristov, G. Urbanik, K. Kummer, D. V. Vyalikh, O. V. Molodtsova, A. B. Preobrajenski, A. A. Zakharov, C. Hess, T. Hänke, B. Büchner, I. Vobornik, J. Fujii, G. Panaccione, Y. A. Ossipyan, and M. Knupfer, "Graphene synthesis on cubic SiC/Si wafers. Perspectives for mass production of graphene-based electronic devices," *Nano Lett.*, vol. 10, no. 3, pp. 992–995, 2010.

[79] D. V. Kosynkin, A. L. Higginbotham, A. Sinitskii, J. R. Lomeda, A. Dimiev, B. K. Price, and J. M. Tour, "Longitudinal unzipping of carbon nanotubes to form graphene nanoribbons," *Nature*, vol. 458, no. 7240, pp. 872–876, 2009.

[80] X. Qi, K. Y. Pu, H. Li, X. Zhou, S. Wu, Q. L. Fan, B. Liu, F. Boey, W. Huang, and H. Zhang, "Amphiphilic graphene composites," *Angew. Chemie - Int. Ed.*, vol. 49, no. 49, pp. 9426–9429, 2010.

[81] D. Li, M. B. Müller, S. Gilje, R. B. Kaner, and G. G. Wallace, "Processable aqueous dispersions of graphene nanosheets," *Nat. Nanotechnol.*, vol. 3, no. 2, pp. 101–105, Feb. 2008.

[82] J. B. Park, W. Xiong, Y. Gao, M. Qian, Z. Q. Xie, M. Mitchell, Y. S. Zhou, G. H. Han, L. Jiang, and Y. F. Lu, "Fast growth of graphene patterns by laser direct writing," *Appl. Phys. Lett.*, vol. 98, no. 12, 2011.

[83] S. Hun, "Thermal Reduction of Graphene Oxide," in *Physics and Applications of Graphene - Experiments*, S. Mikhailov, Ed. InTech, 2011, pp. 73–90.

[84] L. G. Guex, B. Sacchi, K. F. Peuvot, R. L. Andersson, A. M. Pourrahimi, V. Ström, S. Farris, and R. T. Olsson, "Experimental review: chemical reduction of graphene oxide (GO) to reduced graphene oxide (rGO) by aqueous chemistry," *Nanoscale*, vol. 9, no. 27, pp. 9562–9571, 2017.

[85] C. K. Chua and M. Pumera, "Chemical reduction of graphene oxide: a synthetic chemistry viewpoint," *Chem. Soc. Rev.*, vol. 43, no. 1, pp. 291–312, 2014.

[86] H.-L. Guo, X.-F. Wang, Q.-Y. Qian, F.-B. Wang, and X.-H. Xia, "A Green Approach to the Synthesis of Graphene Nanosheets," *ACS Nano*, vol. 3, no. 9, pp. 2653–2659, Sep. 2009.

[87] G. K. Ramesha and S. Sampath, "Electrochemical Reduction of Oriented Graphene Oxide Films: An in Situ Raman Spectroelectrochemical Study," *J. Phys. Chem. C*, vol. 113, no. 19, pp. 7985–7989, May 2009.

[88] M. Zhou, Y. Wang, Y. Zhai, J. Zhai, W. Ren, F. Wang, and S. Dong, "Controlled synthesis of large-area and patterned electrochemically reduced graphene oxide films," *Chem. - A Eur. J.*, vol. 15, no. 25, pp. 6116–6120, 2009.

[89] D. R. Dreyer, S. Park, C. W. Bielawski, and R. S. Ruoff, "The chemistry of graphene oxide," *Chem. Soc. Rev.*, vol. 39, no. 1, pp. 228–240, 2010.

[90] Z. Wang, X. Zhou, J. Zhang, F. Boey, and H. Zhang, "Direct Electrochemical Reduction of Single-Layer Graphene Oxide and Subsequent Functionalization with Glucose Oxidase," *J. Phys. Chem. C*, vol. 113, no. 32, pp. 14071–14075, Aug. 2009.

[91] A. Lamberti, F. Clerici, M. Fontana, and L. Scaltrito, "A highly stretchable supercapacitor using laser-induced graphene electrodes onto elastomeric substrate," *Adv. Energy Mater.*, vol. 6, no. 10, pp. 1–6, 2016.

[92] W. Song, J. Zhu, B. Gan, S. Zhao, H. Wang, C. Li, and J. Wang, "Flexible, Stretchable, and Transparent Planar Microsupercapacitors Based on 3D Porous Laser-Induced Graphene," *Small*, vol. 1702249, pp. 1–7, 2017.

[93] L. X. Duy, Z. Peng, Y. Li, J. Zhang, Y. Ji, and J. M. Tour, "Laser-induced graphene fibers," *Carbon N. Y.*, vol. 126, pp. 472–479, 2018.

[94] Y. Li, D. X. Luong, J. Zhang, Y. R. Tarkunde, C. Kittrell, F. Sargunaraj, Y. Ji, C. J. Arnusch, and J. M. Tour, "Laser-Induced Graphene in Controlled Atmospheres: From Superhydrophilic to Superhydrophobic Surfaces," *Adv. Mater.*, vol. 29, no. 27, pp. 1–8, 2017.

[95] J. Bin In, B. Hsia, J. H. Yoo, S. Hyun, C. Carraro, R. Maboudian, and C. P. Grigoropoulos, "Facile fabrication of flexible all solid-state micro-supercapacitor by direct laser writing of porous carbon in polyimide," *Carbon N. Y.*, vol. 83, pp. 144–151, 2015.

[96] Z. Peng, J. Lin, R. Ye, E. L. G. Samuel, and J. M. Tour, "Flexible and Stackable Laser-Induced Graphene Supercapacitors," *ACS Appl. Mater. Interfaces*, vol. 7, no. 5, pp. 3414–3419, Feb. 2015.

[97] F. Clerici, M. Fontana, S. Bianco, M. Serrapede, F. Perrucci, S. Ferrero, E. Tresso, and A. Lamberti, "In situ MoS2 Decoration of Laser-Induced Graphene as Flexible Supercapacitor Electrodes," *ACS Appl. Mater. Interfaces*, vol. 8, no. 16, pp. 10459–10465, 2016.

[98] Z. Peng, R. Ye, J. A. Mann, D. Zakhidov, Y. Li, P. R. Smalley, J. Lin, and J. M. Tour, "Flexible Boron-Doped Laser-Induced Graphene Microsupercapacitors," *ACS Nano*, vol. 9, no. 6, pp. 5868–5875, 2015.

[99] L. Li, J. Zhang, Z. Peng, Y. Li, C. Gao, Y. Ji, R. Ye, N. D. Kim, Q. Zhong, Y. Yang, H. Fei, G. Ruan,

and J. M. Tour, "High-Performance Pseudocapacitive Microsupercapacitors from Laser-Induced Graphene," *Adv. Mater.*, vol. 28, no. 5, pp. 838–845, 2016.

[100] F. Tehrani and B. Bavarian, "Facile and scalable disposable sensor based on laser engraved graphene for electrochemical detection of glucose," *Sci. Rep.*, vol. 6, no. 1, p. 27975, Sep. 2016.

[101] C. Cheng, S. Wang, J. Wu, Y. Yu, R. Li, S. Eda, J. Chen, G. Feng, B. Lawrie, and A. Hu, "Bisphenol A Sensors on Polyimide Fabricated by Laser Direct Writing for Onsite River Water Monitoring at Attomolar Concentration," *ACS Appl. Mater. Interfaces*, vol. 8, no. 28, pp. 17784–17792, 2016.

[102] A. Nag, S. C. Mukhopadhyay, and J. Kosel, "Sensing system for salinity testing using laser-induced graphene sensors," *Sensors Actuators, A Phys.*, vol. 264, pp. 107–116, 2017.

[103] G. Xu, Z. A. Jarjes, V. Desprez, P. A. Kilmartin, and J. Travas-Sejdic, "Sensitive, selective, disposable electrochemical dopamine sensor based on PEDOT-modified laser scribed graphene," *Biosens. Bioelectron.*, vol. 107, no. February, pp. 184–191, 2018.

[104] X. Xuan, J. Y. Kim, X. Hui, P. S. Das, H. S. Yoon, and J.-Y. Park, "A Highly stretchable and conductive 3D porous graphene metal nanocomposite based electrochemical-physiological hybrid biosensor," *Biosens. Bioelectron.*, vol. 120, no. August, pp. 160–167, 2018.

[105] P. Nayak, N. Kurra, C. Xia, and H. N. Alshareef, "Highly Efficient Laser Scribed Graphene Electrodes for On-Chip Electrochemical Sensing Applications," *Adv. Electron. Mater.*, vol. 2, no. 10, 2016.

[106] S. Luo, P. T. Hoang, and T. Liu, "Direct laser writing for creating porous graphitic structures and their use for flexible and highly sensitive sensor and sensor arrays," *Carbon N. Y.*, vol. 96, pp. 522–531, Jan. 2016.

[107] D. X. Luong, A. K. Subramanian, G. A. L. Silva, J. Yoon, S. Cofer, K. Yang, P. S. Owuor, T. Wang, Z. Wang, J. Lou, P. M. Ajayan, and J. M. Tour, "Laminated Object Manufacturing of 3D-Printed Laser-Induced Graphene Foams," *Adv. Mater.*, vol. 30, no. 28, pp. 1–6, 2018.

[108] C. Fenzl, P. Nayak, T. Hirsch, O. S. Wolfbeis, H. N. Alshareef, and A. J. Baeumner, "Laser-Scribed Graphene Electrodes for Aptamer-Based Biosensing," *ACS Sensors*, vol. 2, no. 5, pp. 616–620, May 2017.

[109] D. C. Vanegas, L. Patiño, C. Mendez, D. A. de Oliveira, A. M. Torres, C. L. Gomes, and E. S. McLamore, "Laser scribed graphene biosensor for detection of biogenic amines in food samples using locally sourced materials," *Biosensors*, vol. 8, no. 2, 2018.

[110] A. R. Cardoso, A. C. Marques, L. Santos, A. F. Carvalho, F. M. Costa, R. Martins, M. G. F. Sales, and E. Fortunato, "Molecularly-imprinted chloramphenicol sensor with laser-induced graphene electrodes," *Biosens. Bioelectron.*, 2018.

[111] M. Barreiros dos Santos, J. P. Agusil, B. Prieto-Simón, C. Sporer, V. Teixeira, and J. Samitier, "Highly sensitive detection of pathogen Escherichia coli O157: H7 by electrochemical impedance spectroscopy," *Biosens. Bioelectron.*, vol. 45, no. 1, pp. 174–180, 2013.

[112] Y. Wang, J. Ping, Z. Ye, J. Wu, and Y. Ying, "Impedimetric immunosensor based on gold nanoparticles modified graphene paper for label-free detection of Escherichia coli O157:H7.," *Biosens. Bioelectron.*, vol. 49, pp. 492–8, 2013.

[113] J. Wan, J. Ai, Y. Zhang, X. Geng, Q. Gao, and Z. Cheng, "Signal-off impedimetric immunosensor for the detection of Escherichia coli O157:H7.," *Sci. Rep.*, vol. 6, p. 19806, 2016.

[114] A. D. Chowdhury, A. De, C. R. Chaudhuri, K. Bandyopadhyay, and P. Sen, "Label free polyaniline based impedimetric biosensor for detection of E. coli O157:H7 Bacteria," *Sensors Actuators, B Chem.*, vol. 171–172, pp. 916–923, 2012.

[115] V. Escamilla-Gómez, S. Campuzano, M. Pedrero, and J. M. Pingarrón, "Gold screen-printed-based impedimetric immunobiosensors for direct and sensitive Escherichia coli quantisation," *Biosens. Bioelectron.*, vol. 24, no. 11, pp. 3365–3371, 2009.

[116] Y. X. Wang, Z. Z. Ye, and Y. B. Ying, "Development of a disposable impedance biosensor and its application for determination of Escherichia coli O157:H7," *Trans. ASABE*, vol. 57, no. 2, pp. 585–591, 2014.

[117] A. Pandey, Y. Gurbuz, V. Ozguz, J. H. Niazi, and A. Qureshi, "Graphene-interfaced electrical biosensor for label-free and sensitive detection of foodborne pathogenic E. coli O157:H7," *Biosens. Bioelectron.*, vol. 91, no. December 2016, pp. 225–231, 2017.

[118] B. Thakur, G. Zhou, J. Chang, H. Pu, B. Jin, X. Sui, X. Yuan, C. H. Yang, M. Magruder, and J. Chen, "Rapid detection of single E. coli bacteria using a graphene-based field-effect transistor device," *Biosens. Bioelectron.*, vol. 110, no. February, pp. 16–22, 2018.

[119] S. Xu, "Electrochemical DNA Biosensor Based on Graphene Oxide- Chitosan Hybrid Nanocomposites for Detection of Escherichia Coli O157:H7," *Int. J. Electrochem. Sci.*, vol. 12, pp. 3443–3458, 2017.

50

[120] A. Shabani, M. Zourob, B. Allain, C. A. Marquette, M. F. Lawrence, and R. Mandeville, "Bacteriophage-modified microarrays for the direct impedimetric detection of bacteria," *Anal. Chem.*, vol. 80, no. 24, pp. 9475–9482, 2008.

[121] J. M. P. Gonçalves, "Laser-induced graphene electrodes for capacitive deionization," Universidade de Aveiro, 2017.

[122] O. J. Guy and K. A. D. Walker, *Graphene Functionalization for Biosensor Applications*, Second Edi. Elsevier Inc., 2016.

[123] J. Landoulsi, M. J. Genet, K. El Kirat, C. Richard, S. Pulvin, and P. G. Rouxhet, "Silanization with APTES for Controlling the Interactions Between Stainless Steel and Biocomponents: Reality vs Expectation," in *Biomaterials – Physics and Chemistry*, R. Pignatello, Ed. InTech, 2011, pp. 99–126.

[124] I. Silva, M. Tacão, R. D. S. Tavares, R. Miranda, S. Araújo, C. M. Manaia, and I. Henriques, "Fate of cefotaxime-resistant Enterobacteriaceae and ESBL-producers over a full-scale wastewater treatment process with UV disinfection," *Sci. Total Environ.*, vol. 639, pp. 1028–1037, 2018.

[125] M. Tacão, S. Araújo, M. Vendas, A. Alves, and I. Henriques, "Shewanella species as the origin of blaOXA-48genes: insights into gene diversity, associated phenotypes and possible transfer mechanisms," *Int. J. Antimicrob. Agents*, vol. 51, no. 3, pp. 340–348, 2018.

[126] A. C. Ferrari and D. M. Basko, "Raman spectroscopy as a versatile tool for studying the properties of graphene," *Nat. Nanotechnol.*, vol. 8, no. 4, pp. 235–246, Apr. 2013.

[127] A. C. Ferrari, "Raman spectroscopy of graphene and graphite: Disorder, electron–phonon coupling, doping and nonadiabatic effects," *Solid State Commun.*, vol. 143, no. 1–2, pp. 47–57, Jul. 2007.

[128] A. C. Ferrari, J. C. Meyer, V. Scardaci, C. Casiraghi, M. Lazzeri, F. Mauri, S. Piscanec, D. Jiang, K. S. Novoselov, S. Roth, and A. K. Geim, "Raman Spectrum of Graphene and Graphene Layers," *Phys. Rev. Lett.*, vol. 97, no. 18, p. 187401, Oct. 2006.

[129] R. Rao, R. Podila, R. Tsuchikawa, J. Katoch, D. Tishler, A. M. Rao, and M. Ishigami, "Effects of Layer Stacking on the Combination Raman Modes in Graphene," *ACS Nano*, vol. 5, no. 3, pp. 1594–1599, Mar. 2011.

[130] A. Eckmann, A. Felten, A. Mishchenko, L. Britnell, R. Krupke, K. S. Novoselov, and C. Casiraghi, "Probing the nature of defects in graphene by Raman spectroscopy," *Nano Lett.*, vol. 12, no. 8, pp. 3925–3930, 2012.

[131] P. G. Spizzirri, J. H. Fang, S. Rubanov, E. Gauja, and S. Prawer, "Nano-Raman spectroscopy of silicon surfaces," *Mater. Forum*, vol. 34, pp. 161–166, 2008.

[132] J. E. O'Reilly, "Oxidation-reduction potential of the ferro-ferricyanide system in buffer solutions," *BBA - Bioenerg.*, vol. 292, no. 3, pp. 509–515, 1973.

[133] M. Orazem and B. Tribollet, "Electrochemical Impedance Spectroscopy," *Annu. Rev. Anal. Chem.*, pp. 2017–229, 2010.

[134] H. L. Poh and M. Pumera, "Nanoporous Carbon Materials for Electrochemical Sensing," *Chem. - An Asian J.*, vol. 7, no. 2, pp. 412–416, Feb. 2012.

[135] M. C. Granger, M. Witek, J. Xu, J. Wang, M. Hupert, A. Hanks, M. D. Koppang, J. E. Butler, G. Lucazeau, M. Mermoux, J. W. Strojek, and G. M. Swain, "Standard Electrochemical Behavior of High-Quality, Boron-Doped Polycrystalline Diamond Thin-Film Electrodes," *Anal. Chem.*, vol. 72, no. 16, pp. 3793–3804, Aug. 2000.

[136] L. Tang, Y. Wang, Y. Li, H. Feng, J. Lu, and J. Li, "Preparation, Structure, and Electrochemical Properties of Reduced Graphene Sheet Films," *Adv. Funct. Mater.*, vol. 19, no. 17, pp. 2782–2789, Sep. 2009.

[137] A. T. Valota, I. A. Kinloch, K. S. Novoselov, C. Casiraghi, A. Eckmann, E. W. Hill, and R. A. W. Dryfe, "Electrochemical Behavior of Monolayer and Bilayer Graphene," *ACS Nano*, vol. 5, no. 11, pp. 8809–8815, Nov. 2011.

[138] C. Punckt, M. A. Pope, and I. A. Aksay, "On the Electrochemical Response of Porous Functionalized Graphene Electrodes," *J. Phys. Chem. C*, vol. 117, no. 31, pp. 16076–16086, Aug. 2013.

[139] J. M. Nugent, K. S. V Santhanam, A. Rubio, and P. M. Ajayan, "Fast Electron Transfer Kinetics on Multiwalled Carbon Nanotube Microbundle Electrodes," *Nano Lett.*, vol. 1, no. 2, pp. 87–91, Feb. 2001.

[140] A. W. Bott and W. R. Heineman, "Chronocoulometry," *Curr. Sep.*, vol. 20, no. 4, pp. 121–126, 2004.

[141] F. Wang, K. Wang, X. Dong, X. Mei, Z. Zhai, B. Zheng, J. Lv, W. Duan, and W. Wang, "Formation of hierarchical porous graphene films with defects using a nanosecond laser on polyimide sheet," *Appl. Surf. Sci.*, vol. 419, pp. 893–900, 2017.

[142] S. P. Singh, Y. Li, A. Be'Er, Y. Oren, J. M. Tour, and C. J. Arnusch, "Laser-Induced Graphene Layers

and Electrodes Prevents Microbial Fouling and Exerts Antimicrobial Action," *ACS Appl. Mater. Interfaces*, vol. 9, no. 21, pp. 18238–18247, 2017.

[143] L. Lai, L. Chen, D. Zhan, L. Sun, J. Liu, S. H. Lim, C. K. Poh, Z. Shen, and J. Lin, "One-step synthesis of NH2-graphene from in situ graphene-oxide reduction and its improved electrochemical properties," *Carbon N. Y.*, vol. 49, no. 10, pp. 3250–3257, 2011.

[144] S. Muralikrishna, K. Sureshkumar, T. S. Varley, D. H. Nagaraju, and T. Ramakrishnappa, "In situ reduction and functionalization of graphene oxide with L-cysteine for simultaneous electrochemical determination of cadmium(II), lead(II), copper(II), and mercury(II) ions," *Anal. Methods*, vol. 6, no. 21, pp. 8698–8705, 2014.

[145] J. Wang, C. Wang, H. Shen, and S. Chen, "Fabrication of pH-sensitive GO-Grug Supramolecular Hydrogels as Controlled Release," vol. 2, no. c, pp. 1–4, 2010.

[146] B. Li, "Graphene transistors for label-free biosensing," University of Plymouth, 2016.

[147] S. Teixeira, G. Burwell, A. Castaing, D. Gonzalez, R. S. Conlan, and O. J. Guy, "Epitaxial graphene immunosensor for human chorionic gonadotropin," *Sensors Actuators, B Chem.*, vol. 190, pp. 723–729, 2014.

[148] D. C. Elias, R. R. Nair, T. M. G. Mohiuddin, S. V. Morozov, P. Blake, M. P. Halsall, A. C. Ferrari, D. W. Boukhvalov, M. I. Katsnelson, A. K. Geim, and K. S. Novoselov, "Control of Graphene's Properties by Reversible Hydrogenation: Evidence for Graphane," *Science (80-.).*, vol. 323, no. 5914, pp. 610–613, Jan. 2009.

[149] S. V. Harb, B. M. Cerrutti, S. H. Pulcinelli, C. V. Santilli, and P. Hammer, "Siloxane-PMMA hybrid anti-corrosion coatings reinforced by lignin," *Surf. Coatings Technol.*, vol. 275, no. May, pp. 9–16, 2015.

[150] R. Dahiya, G. Gottardi, and N. Laidani, "PDMS residues-free micro/macrostructures on flexible substrates," *Microelectron. Eng.*, vol. 136, pp. 57–62, 2015.

[151] A. Al-Kattan, Y. V. Ryabchikov, T. Baati, V. Chirvony, J. F. Sánchez-Royo, M. Sentis, D. Braguer, V. Y. Timoshenko, M. A. Estève, and A. V. Kabashin, "Ultrapure laser-synthesized Si nanoparticles with variable oxidation states for biomedical applications," *J. Mater. Chem. B*, vol. 4, no. 48, pp. 7852–7858, 2016.

[152] N. T. Sl, "Reduced Graphene-Oxide-NH2 Characterization Sheet," pp. 2–4, 2000.

[153] Q. Zheng, X. Cheng, and H. Li, "Microwave Synthesis of High Activity FeSe2/C Catalyst toward Oxygen Reduction Reaction," *Catalysts*, vol. 5, no. 3, pp. 1079–1091, Jun. 2015.

[154] S. R. Darmakkolla, H. Tran, A. Gupta, and S. B. Rananavare, "A method to derivatize surface silanol groups to Si-alkyl groups in carbon-doped silicon oxides," *RSC Adv.*, vol. 6, no. 95, pp. 93219–93230, 2016.

[155] A. G. Kochur, T. M. Ivanova, A. V. Shchukarev, R. V. Linko, A. A. Sidorov, M. A. Kiskin, V. M. Novotortsev, and I. L. Eremenko, "X-ray photoelectron Fe3s and Fe3p spectra of polynuclear trimethylacetate iron complexes," *J. Electron Spectros. Relat. Phenomena*, vol. 180, no. 1–3, pp. 21–26, 2010.

[156] T. Influence and B. Sites, "AFM and XPS Study of Aminosilanes on Si," pp. 3–6, 2014.

[157] Z. Sun, Y. An, H. Li, H. Zhu, and M. Lu, "Electrochemical Investigation of Testosterone Using a AuNPs Modified Electrode," vol. 12, pp. 11224–11234, 2017.

[158] N. Puri, V. Sharma, V. K. Tanwar, N. Singh, and A. M. Biradar, "Enzyme-modified indium tin oxide microelectrode array-based electrochemical uric acid biosensor," *Prog. Biomater.*, vol. 2, no. 1, p. 5, 2013.

[159] M. Ç. Canbaz and M. K. Sezgintürk, "Fabrication of a highly sensitive disposable immunosensor based on indium tin oxide substrates for cancer biomarker detection," *Anal. Biochem.*, vol. 446, no. 1, pp. 9–18, 2014.

[160] S. Kumar, S. Kumar, C. M. Pandey, and B. D. Malhotra, "Conducting paper based sensor for cancer biomarker detection," *J. Phys. Conf. Ser.*, vol. 704, no. 1, pp. 0–9, 2016.

[161] S. K. Mishra, A. K. Srivastava, and Devendra Kumar b and Rajesh a*, "Bio-functionalized Pt nanoparticles based electrochemical impedance immunosensor for human cardiac myoglobin."

[162] C. T. Bot and C. Prodan, "Quantifying the membrane potential during E. coli growth stages," *Biophys. Chem.*, vol. 146, no. 2–3, pp. 133–137, Feb. 2010.

[163] D. Zilberstein, V. Agmon, S. Schuldiner, and E. Padan, "Escherichia coli intracellular pH, membrane potential, and cell growth," *J. Bacteriol.*, vol. 158, no. 1, pp. 246–252, 1984.